Monthly Notices of the ROYAL ASTRONOMICAL SOCIETY

MNRAS **534,** 883–901 (2024) https://doi.org/10.1093/mnras/stae2119
Advance Access publication 2024 September 11

Quantifying azimuthal variations within the interstellar medium of $z \sim 0$ spiral galaxies with the TYPHOON survey

Qian-Hui Chen (千惠陈) [1,2]★ Kathryn Grasha [1,2,3]† Andrew J. Battisti [1,2] Emily Wisnioski [1,2] Zefeng Li (泽峰李) [1,2,4] Hye-Jin Park [1,2] Brent Groves [2,5] Paul Torrey [6] Trevor Mendel [1,2] Barry F. Madore [7,8] Mark Seibert [7] Eva Sextl [9] Alex M. Garcia [6] Jeff A. Rich [7] Rachael L. Beaton [7,10]‡ and Lisa J. Kewley [1,2,11]

[1]*Research School of Astronomy and Astrophysics, Australian National University, Canberra, ACT 2611, Australia*
[2]*ARC Centre of Excellence for All Sky Astrophysics in 3 Dimensions (ASTRO 3D), Australia*
[3]*Visiting Fellow, Harvard-Smithsonian Center for Astrophysics, 60 Garden Street, Cambridge, MA 02138, USA*
[4]*Centre for Extragalactic Astronomy, Department of Physics, Durham University, South Road, Durham DH1 3LE, UK*
[5]*International Centre for Radio Astronomy Research, University of Western Australia, 35 Stirling Highway, Crawley WA 6009, Australia*
[6]*Department of Astronomy, University of Virginia, Charlottesville, VA 22904, USA*
[7]*The Observatories, Carnegie Institution for Science, 813 Santa Barbara Street, Pasadena, CA 91106, USA*
[8]*Department of Astronomy and Astrophysics, University of Chicago, Chicago, IL 60637, USA*
[9]*Fakultät für Physik, Ludwig-Maximilians Universität München, Universitäts-Sternwarte, Scheinerstraße 1, D-81679 München, Germany*
[10]*Department of Astrophysical Sciences, 4 Ivy Lane, Princeton University, Princeton, NJ 08544, USA*
[11]*Institute for Theory and Computation, Harvard-Smithsonian Center for Astrophysics, Cambridge, MA 02138, USA*

Accepted 2024 September 5. Received 2024 September 5; in original form 2024 March 28

ABSTRACT

Most star formation in the local Universe occurs in spiral galaxies, but their origin remains an unanswered question. Various theories have been proposed to explain the development of spiral arms, each predicting different spatial distributions of the interstellar medium. This study maps the star formation rate (SFR) and gas-phase metallicity of nine spiral galaxies with the TYPHOON survey to test two dominating theories: density wave theory and dynamic spiral theory. We discuss the environmental effects on our galaxies, considering reported environments and merging events. Taking advantage of the large field of view covering the entire optical disc, we quantify the fluctuation of SFR and metallicity relative to the azimuthal distance from the spiral arms. We find higher SFR and metallicity in the trailing edge of NGC 1365 (by 0.117 and 0.068 dex, respectively) and NGC 1566 (by 0.119 and 0.037 dex, respectively), which is in line with density wave theory. NGC 2442 shows a different result with higher metallicity (0.093 dex) in the leading edge, possibly attributed to an ongoing merging. The other six spiral galaxies show no statistically significant offset in SFR or metallicity, consistent with dynamic spiral theory. We also compare the behaviour of metallicity inside and outside the corotation radius (CR) of NGC 1365 and NGC 1566. We find comparable metallicity fluctuations near and beyond the CR of NGC 1365, indicating gravitational perturbation. NGC 1566 shows the greatest fluctuation near the CR, in line with the analytic spiral arms. Our work highlights that a combination of mechanisms explains the origin of spiral features in the local Universe.

Key words: ISM: evolution – galaxies: abundances – galaxies: evolution – galaxies: ISM – galaxies: spiral.

1 INTRODUCTION

Spiral galaxies constitute approximately two-thirds of all massive galaxies in the local Universe (Lintott et al. 2008; Willett et al. 2013) and are the primary hosts for most star formation (Brinchmann et al. 2004). Despite their ubiquity, the underlying physics that drives the origin of spiral features remains a topic of ongoing debate. Numerous previous studies over the past decades have endeavoured to explain the formation of spiral arms through various theoretical frameworks (Lin & Shu 1964; Toomre 1977; Athanassoula 1992; Binney & Tremaine 2008).

Among all the proposed theories, the three most widely accepted ones are the density wave theory, dynamic spiral theory, and tidal-induced spiral arms. While the proposed mechanisms may potentially all contribute to the formation and evolution of spiral features in a galaxy, each has specific characteristics that we detail below:

(Quasi-stationary) density wave theory. Proposed by Lin & Shu (1964), later improved and popularized by Toomre (1977), Bertin & Lin (1996), and Shu (2016), the density wave theory envisages

★ E-mail: Qianhui.Chen@anu.edu.au
† ARC DECRA Fellow
‡ Hubble Fellow

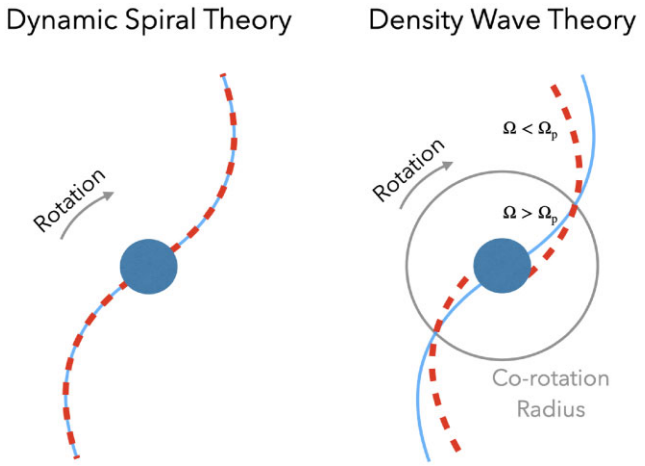

Figure 1. Theoretical expectations from the dynamic spiral theory (left) and density wave theory (right) regarding the location of young (blue solid) and old (red dashed) stellar populations. The azimuthal offset between young and old stars is predicted by density wave theory but not by dynamic spiral theory, also see fig. 1 in Puerari & Dottori (1997) and Martínez-García, González-López lira & Bruzual-A (2009). The rotation direction is based on the assumption that the observed spiral arms are trailing features, which will be applied to all spiral galaxies in this work. Ω refers to the rotational velocity of material, while Ω_p denotes the rotational velocity of the spiral pattern.

long-lived spiral arms and solves the winding problem.[1] This theory proposes that spiral features are areas of greater density that rotate at a specific pattern speed across the disc, and the differential gravitational pull leads to a logarithmic spiral with a constant pitch angle (Athanassoula et al. 2010; Martínez-García 2012; Davis et al. 2015). As the pattern speed of the spiral arms is constant, while the rotational velocity of the stars varies radially, differential rotation occurs (right panel of Fig. 1). Only at the corotation radius (CR) are the stars and the arms expected to rotate synchronously. Due to differential rotation, the new-borne stars rotate faster than the spiral pattern within the CR while falling behind outside the CR, which has been observed in previous works (Pour-Imani et al. 2016; Peterken et al. 2019). Thus in this theory, the interstellar medium (ISM) properties and stellar populations differ on the leading and trailing edges of the spiral arms (Gittins & Clarke 2004). Ho et al. (2017) observe lower gas-phase metallicity in the leading edge than the trailing edge in NGC 1365, which can be explained by their toy model.

Dynamic spiral theory. Sellwood & Carlberg (1984) suggest that spiral arms are short-lived and recurrent features. In numerical simulations, dynamic spiral arms arise rapidly from gravitational instability due to swing amplification (Fujii et al. 2011; Grand, Kawata & Cropper 2012; D'Onghia, Vogelsberger & Hernquist 2013). However, this kind of spiral arms fades quickly because of the particle scattering and increased velocity dispersion of stars in the simulations. The spiral arms heat the disc kinematically and undergo a cycle of breaking up into small segments of kpc in size. The segments possibly will reconnect to form new, large-scale spiral patterns, which makes the spiral features 'recurrent'. While the dynamic spiral arms may appear globally cohesive, the assemblies of segments can form at distinct times and later merge with the arms. This contrasts with density wave theory, where the spiral arms arise as an entity. A kinematically cold population of stars help maintain the dynamic spiral arms while gas dissipation and accretion introduce instabilities. There is no significant difference in rotation between the disc and the dynamic spiral arms. Thus, the stars do not flow across the spiral features but stay still in the arm regions due to gravitational potential. This means no coherent azimuthal variations are expected between the gas and stars in dynamical spiral theory (left panel of Fig. 1).

Tidal-induced spiral arms. Tidal interactions are common and give rise to tails, bridges, and spiral features (Pfleiderer & Siedentopf 1961; Pikel'Ner 1965; Toomre & Toomre 1972). Toomre (1969) predict that the outer arms and tidal tails are material arms, rotating at a similar angular velocity with the disc, which is observed in M51 (Meidt et al. 2013). However, some simulations (Sundelius et al. 1987) and observations (Rots & Shane 1975) argue that tidal-induced spiral arms are density waves. Interestingly, the density wave spiral arms from tidal interactions can be quasi-stationary or kinematic – the gas and stars do flow through the spiral arms but the spiral pattern speed decreases with radii (Donner & Thomasson 1994; Oh, Kim & Lee 2015). Simulations (Pettitt, Tasker & Wadsley 2016; Pettitt et al. 2017) report that azimuthal offsets do exist in different media in a tidal-induced spiral galaxy, in agreement with observations (Schinnerer et al. 2013; Egusa et al. 2017).

The fundamental physics that drives the formation of spiral features remains a topic of debate, given the various observational results among different spiral galaxies in our Universe. One of the practical methods to discern the dominant theory is to detect the azimuthal variation across the spiral arms – as the density wave theory predicts an observable azimuthal offset in ISM properties such as gas-phase metallicity and stellar ages while dynamic spiral theory predicts no offset. However, existing observational evidence is conflicted with clear azimuthal variations in metallicities seen in some galaxy samples (Sánchez-Menguiano et al. 2016; Ho et al. 2017, 2018; Vogt et al. 2017), but not in others (e.g. Foyle et al. 2011; Kreckel et al. 2019; Chen et al. 2024). The discrepancy also occurs in stellar ages with some galaxies showing azimuthal variation (Martínez-García et al. 2009; Sánchez-Gil et al. 2011; Abdeen et al. 2022) and others not (Choi et al. 2015; Shabani et al. 2018). More studies using multiwavelength imaging data report the offset between the young and old stellar populations (Egusa, Sofue & Nakanishi 2004; Egusa et al. 2009; Pour-Imani et al. 2016; Yu & Ho 2019; Abdeen et al. 2020; Savchenko et al. 2020), in line with density wave theory.

For isolated spiral galaxies, density wave and dynamic spiral theory are two widely accepted mechanisms driving the spiral features. However, tidal forces from interactions with passing or nearby companions can also give rise to spiral arms with an offset between the gas and the stars (Pettitt et al. 2017), making it more difficult to test density wave theory or dynamic spiral theory. Conversely, tidal-induced spiral galaxies show distinct behaviours in their tail and bridge arms. Gravity perturbations from the interaction can create two-armed spiral galaxies (Toomre & Toomre 1972; Pettitt & Wadsley 2018), which is likely the case in M51 (Dobbs et al. 2010). Spiral features created in tidal interactions are more likely to be kinematic density waves (Binney & Tremaine 1987, ch. 6) that will wind up faster than quasi-stationary density waves. However, the gas moves through the spiral arms from the trailing edge to the leading edge, similar to the quasi-stationary density waves (Oh et al. 2008; Struck, Dobbs & Hwang 2011). These findings indicate that the ISM and stellar distributions in spiral galaxies may be under the impact of more than one physical mechanism.

[1]The winding problem: in other theories, the pitch angle of the spiral features is expected to decrease to 0 over time, which is in disagreement with observations of long-lived spirals.

With three common theories briefly explained, we summarize the expectations of star formation surface density ($\Sigma_{\rm SFR}$) and gas-phase metallicity in observation from the different mechanisms. In density wave theory, the spiral arms observed in shorter wavelengths, where the most recent star formation event has occurred, should exhibit a looser pitch angle (blue arms in the right panel of Fig. 1) than the spiral arms observed in redder wavelengths, dominated by the old stars (Pour-Imani et al. 2016). If star formation occurs after gas clouds pass through the minimum potential of density waves (left spiral arm in fig. 1 of Pour-Imani et al. 2016), the peaks of $\Sigma_{\rm SFR}$ are predicted in the leading edge inside the CR (Martínez-García et al. 2009). If star formation starts as the gas clouds approach the density wave (right spiral arm in fig. 1 of Pour-Imani et al. 2016), $\Sigma_{\rm SFR}$ should be higher in the trailing edge inside the CR. In contrast, the dynamic spiral theory predicts a symmetrical $\Sigma_{\rm SFR}$ distribution to the spiral arms. Tidal induced-spiral structures will lead to kinematic density waves which result in azimuthal variations, exhibiting a decreasing pattern speed with increasing radii. The comparison of $\Sigma_{\rm SFR}$ between the leading and trailing edge, combined with the reported environmental factors, will help to disentangle the origin of spiral features.

For gas-phase metallicity, spiral arms driven by density wave theory will lead to higher metallicity in the trailing edge than the leading edge, within the CR. This scenario is modelled in Ho et al. (2017) as (1) self-enrichment in the trailing edge before the material reaches the spiral arms, and (2) metal mixing in the leading edge. In dynamic spiral theory, gas-phase metallicity is expected to be symmetric on both sides of the spiral arms, as there is no differential rotation between the spiral arms and the disc.

Although many spiral galaxies in the local Universe and at higher redshift have been studied, most researches (i) focus on H II regions (e.g. Rozas, Knapen & Beckman 1996; Santoro et al. 2022); (ii) examined azimuthal variations through visual comparison on 2D maps (Kreckel et al. 2019), or by binning the spaxels into leading and trailing sections (Ho et al. 2018; Chen et al. 2024). These previous studies offer limited quantitative analysis of the behaviour of the gas and stars as they move away from the spiral arms. In this work, we present the azimuthal distributions of star formation rate (SFR) and gas-phase metallicity and test the toy model in Ho et al. (2017), with a sample of nine nearby spiral galaxies. Our motivation is to quantitatively track the fluctuation in the ISM properties when moving in/out of the spiral arms.

We introduce our observations and sample in Section 2. We present our analysis including spiral arm definition and mapping the ISM properties in Section 3. We report the fluctuation of the ISM properties when moving through the spiral arms in Section 4. In Section 5, we will discuss the effects of CR on our results and the dominant mechanism(s) responsible for driving the spiral features in these galaxies. Luminosity distances are adopted from Leroy et al. (2019), assuming $H_0 = 70$ km s^{-1}Mpc^{-1} and a flat cosmology with $\Omega_m = 0.27$.

2 OBSERVATIONS AND SAMPLE SELECTION

2.1 Observations

TYPHOON[2] is a pseudo-integral field units (IFU) survey of 44 galaxies observable in the Southern hemisphere. TYPHOON uses the wide-field CCD imaging spectrograph (18 arcmin × 1.65 arcsec) on the 2.5-m du Pont telescope at the Las Campanas Observatory in Chile. The TYPHOON survey builds up a dispersed image data cube by applying the Progressive Integral Step Method (PrISM), also known as the 'step-and-stare' technique. The large field of view (FoV) of TYPHOON, ranging from 2.3 arcmin × 18 arcmin to 6.5 arcmin × 18 arcmin in our selected spiral galaxies, allows us to observe the entire optical disc of nearby star-forming galaxies in an IFU-like manner. The spectrograph is configured to have a resolving power of approximately $R\approx 850$ at 7000 Å and $R\approx 960$ at 5577 Å. Our spectra cover the wavelength range of 3650−8150 Å with a flux calibration accuracy of 2 per cent (Ho et al. 2017). The observations are conducted only when the seeing is smaller than the slit width of 1.65 arcsec (to prevent slit loss; Grasha et al. 2022). More detailed information about the TYPHOON/PrISM survey is in Ho et al. (2017), Chen et al. (2023), and Seibert et al. (in preparation). The raw data are reduced into 3D data cubes using a standard long-slit data reduction procedure (Seibert et al. in preparation). The reduced 2D spectra are later tiled together to form 3D data cubes with spectral and spatial samplings of 1.5 Å and 1.65 arcsec, respectively. The astrometric solutions are made for combined slit steps of individual nights independently and they are tied to the *Gaia* reference system (Gaia Collaboration 2016).

2.2 Sample selection

Our work includes bright ($M_{\rm v} < -20$ mag) spiral galaxies that have three spiral arms or fewer. We exclude flocculent galaxies with poorly defined arms to allow for better comparison between leading and trailing regions. We exclude one galaxy (NGC 1068) with more than 20 per cent spaxels impacted by harder component ionization (e.g. active galactic nuclei, AGNs; Lamastra et al. 2016; D'Agostino et al. 2018), based on the Baldwin, Phillips, and Terlevich diagram (BPT diagram; Baldwin, Phillips & Terlevich 1981). The remaining spiral galaxies in our sample show < 2 per cent of their spaxels dominated by AGN (column 12 of Table 1). These selection criteria reduce the total sample to nine well-defined, star-forming galaxies available in this work. Two galaxies have a strong bar (*Hubble* type of SB) and seven galaxies exhibit a weak bar (*Hubble* type of SAB). We constrain our analysis of azimuthal variation starting from/beyond the end of bars (Section 3.3) to focus on the study of spiral arms. The detailed physical parameters are listed in Table 1.

The large FoV allows us to cover the disc regions extending beyond R_{25} for our entire sample. Our sample spans a resolution of 52 − 170 pc pixel^{-1} (1.65 arcsec pixel^{-1}), enabling us to (1) identify the central ridge line of each spiral arm, and (2) measure changes in the ISM when moving azimuthally from the spiral arms on a spaxel level. These azimuthal distributions are key observables to distinguish between competing spiral theories.

3 DATA ANALYSIS

In this section, we introduce our analyses on the TYPHOON data, starting with the emission-line fitting process using LZIFU (Section 3.1). We select reliable spaxels with signal-to-noise ratio (SNR) limits and subsequently identify star-forming spaxels with the BPT diagram, described in Section 3.2. Section 3.3 introduces the methodology to define the ridge lines of the spiral arms. Section 3.4 outlines how we measure the ISM properties ($\Sigma_{\rm SFR}$ and gas-phase metallicity).

3.1 Emission-line fitting

We measure the 2D emission-line maps using the tool LZIFU (Ho 2016; Ho et al. 2016). The reduced emission-line maps of all

[2]https://typhoon.datacentral.org.au/

Table 1. Physical parameters of the spiral galaxies in this study.

Galaxy (1)	T-type (2)	Morphology (3)	RA (4)	Dec. (5)	Inclination (deg) (6)	PA (deg) (7)	Distance (Mpc) (8)	log M_* ($M_\odot$) (9)	R_{25} (arcmin) (10)	Number of spiral arms (11)	Fraction of excluded spaxels (per cent) (12)
NGC 1365	3.2 ± 0.7	SB(s)b	03h33m36.371s	−36d08m25.45s	35.7	49.5	18.1 ± 0.04	10.75 ± 0.10	5.61	2	1.11
NGC 1566	4.0 ± 0.2	SAB(s)bc	04h20m00.42s	−54d56m16.1s	49.1	44.2	18.0 ± 0.12	10.67 ± 0.10	4.16	2	1.14
NGC 2442	3.7 ± 0.6	SAB(s)bc	07h36m23.84s	−69d31m51.0s	50.3	12.3	21.2 ± 2.0	10.56 ± 0.12[a]	2.75	2	0.81
NGC 2835	5.0 ± 0.4	SB(rs)c	09h17m52.91s	−22d21m16.8s	56.2	1.3	10.1 ± 0.12	9.67 ± 0.10	3.30	3	0.05
NGC 2997	5.1 ± 0.5	SAB(rs)c	09h45m38.79s	−31d11m27.9s	53.7	98.9	11.3 ± 0.12	10.46 ± 0.10	4.46	3	0.19
NGC 4536	4.3 ± 0.7	SAB(rs)bc	12h34m27.050s	+ 02d11m17.29s	73.1	120.7	15.2 ± 0.06	10.19 ± 0.10	3.80	3	0.60
NGC 5236	5.0 ± 0.3	SAB(s)c	13h37m00.950s	−29d51m55.50s	15.3	44.9	4.9 ± 0.04	10.41 ± 0.10	6.44	2	0.18
NGC 5643	5.0 ± 0.3	SAB(rs)c	14h32m40.743s	−44d10m27.86s	29.6	98.1	11.8 ± 0.12	10.06 ± 0.10	2.29	2	3.58
NGC 6744	4.0 ± 0.2	SAB(r)bc	19h09m46.10s	−63d51m27.1s	53.5	13.7	11.6 ± 0.12	10.87 ± 0.10	9.98	3	0.66

Notes. Column 1: galaxy name. Column 2: RC3 morphological T-types from Hyperleda (http://atlas.obs-hp.fr/hyperleda/). Columns 3–5**:** morphology and J2000 Coordinates from NASA extragalactic database (NED). Column 6: inclination between the line of sight and polar axis from Hyperleda. Column 7: position angle of the major axis in the *B* band, northeastward[b]. Columns 8 and 9: distance and stellar mass from Leroy et al. (2019). Column 10: R_{25}, defined as the 25 mag arcsec^2*B*-band isophote from NED. Column 11: number of spiral arms in each galaxy (Section 3.3). Column 12: fraction of spaxels excluded from BPT constraints. (Section 3.2).

[a] The stellar mass and the uncertainty of NGC 2442 are from Pan et al. (2020).

[b] The position angle of NGC 1365 comes from the Two Micron All Sky Survey (2MASS) survey (Jarrett et al. 2003), for consistency with Ho et al. (2017).

galaxies in the TYPHOON survey are described in Battisti et al. (in preparation). We briefly introduce the emission-line fitting process of LZIFU below that is relevant to this work.

First, LZIFU uses PPXF (Cappellari & Emsellem 2004; Cappellari 2017) to fit and subtract the continuum on a spaxel-to-spaxel basis. This continuum modelling is based on the MIUSCAT simple stellar population models (Vazdekis et al. 2012). The principle goal of LZIFU is to derive emission lines from continuum-free spectra, rather than constraining stellar parameters from continuum measurements (section 2.2 in Ho 2016).[3] For this work, we only adopt the emission-line fits from LZIFU. Secondly, LZIFU fits each emission line as a single Gaussian component using the Levenberg–Marquardt least-squares method. In this study, we fit the following emission lines simultaneously: Hβ (4861 Å), [O III]λ5007, [N II]λ6583, Hα (6563 Å), and [S II]$\lambda\lambda$6716,31. We tie together the velocity and velocity dispersion of all the lines. The flux ratios of [O III]λ5007/[O III]λ4959 and [N II]λ6583/[N II]λ6548 are constrained to their theoretical values predicted by quantum mechanics (3.1; Gurzadyan 1997). Finally, LZIFU returns the outputs of emission-line fluxes with corresponding error maps.

3.2 Spaxel selection criteria

We apply an SNR limit of 3 to Hα and Hβ to obtain a reliable analysis. The spaxels with SNR (Hα and Hβ) below 3 are excluded from all the following analyses. If an SNR less than 3 is detected in a spaxel for any of the following three doublet lines: [O III]λ5007, [N II]$\lambda\lambda$6548,83 and [S II]$\lambda\lambda$6716,31, we adopt a limiting value of 3σ for the corresponding emission line(s), where σ is the uncertainty in the line measurement (see section 2.6 of Rosario et al. 2016).

We correct for dust extinction using the Milky Way extinction curve from Fitzpatrick et al. (2019) as:

$$E(B-V) = 2.5 \times \left(\frac{\log_{10} \frac{(\mathrm{H}\alpha/\mathrm{H}\beta)_{\mathrm{obs}}}{(\mathrm{H}\alpha/\mathrm{H}\beta)_{\mathrm{int}}}}{k_{\mathrm{H}\beta} - k_{\mathrm{H}\alpha}} \right), \quad (1)$$

where $E(B-V)$ is the colour excess and $(\mathrm{H}\alpha/\mathrm{H}\beta)_{\mathrm{obs}}$ is the observed flux ratio measured from the data. We adopt the intrinsic flux ratio $(\mathrm{H}\alpha/\mathrm{H}\beta)_{\mathrm{int}}$ of 2.86 by assuming case B recombination at the electron temperature of 10 000 K and electron density of 100 cm^{-3} (Osterbrock 1989). We use $R_v = 3.1$ to determine the k value at each wavelength. For spaxels with negative $E(B-V)$ values, we assign a value of 0 to colour excess. The $E(B-V)$ values are then used to calculate the intrinsic emission-line fluxes F_{int} from the observed fluxes F_{obs}, following Calzetti (2001):

$$F_{\mathrm{int}} = F_{\mathrm{obs}} \times 10^{0.4 k_\lambda E(B-V)}. \quad (2)$$

The extinction-corrected fluxes are used in all the following analyses to measure the Σ_{SFR} and gas-phase metallicities (Section 3.4).

We further exclude the spaxels ionized by hard components and limit our study to the photoionized spaxels by star formation by using the BPT diagram. Based on [N II]λ6584/Hα versus [O III]λ5007/Hβ, the spaxels dominantly ionized by star formation (H II regions) are distinguished from the low-ionization nuclear emission-line regions (LINERs) and AGN.

There are two common demarcation lines to separate AGN/LINERs and H II regions based on optical emission lines. Kauffmann et al. (2003) present an empirical demarcation line based on the properties of $\sim$ 120 000 nearby galaxies with the Sloan Digital Sky Survey. Kewley et al. (2001) model the starburst galaxies with PEGASE V2.0 and STARBURST99 to derive the theoretical classification scheme for AGN and H II regions. All spaxels over the Kewley et al. (2001) demarcation line are excluded in the following analysis in this work. The fraction of excluded spaxels due to BPT constraints is below 4 per cent in all cases, as shown in the last column in Table 1.

3.3 Spiral arm definition and $\Delta\phi$ definition

We follow the method of Ho et al. (2018) to identify our spiral arm ridge lines:

$$r(\phi) = r_0 e^{\tan\theta_{\mathrm{p}}(\phi-\phi_0)}, \quad (3)$$

where θ_{p} is the pitch angle, r_0 is the initial radius, and ϕ_0 is the initial azimuth of the spiral arm. The spiral arms are recovered as straight lines in a plot of logarithm-scale deprojected radial distance versus azimuth (Fig. 2). Equation (3) is transformed into a linear

[3] A detailed analysis of stellar populations based on the TYPHOON data is published in Sextl et al. (2024). In this work, continuum fits are conducted at the spaxel level. Hβ absorption line is the only stellar absorption feature that can impact the emission flux. However, Hβ will not be used in our measurements of SFR or 12 + log(O/H).

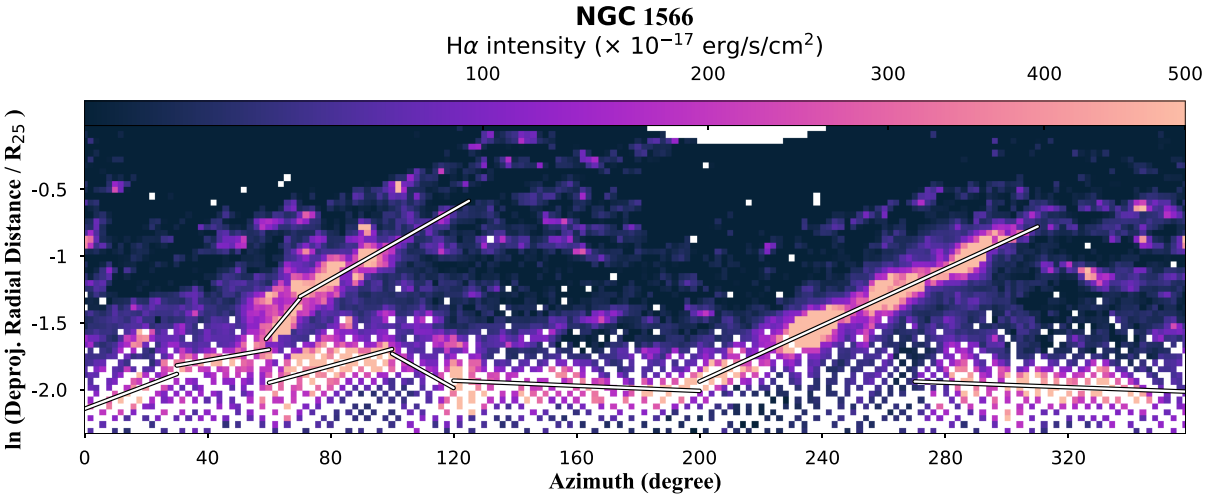

Figure 2. Deprojected radial distance in a logarithm scale versus the azimuth, colour-coded by the Hα intensity of NGC 1566. The best fits of the Hα-bright (intensity $>100 \times 10^{-17}$ erg s^{-1} cm^{-2}) regions are shown as the white solid lines. The pixelation at the central region results from the reduced area as the radial distance decreases.

function:

$$\ln r(\phi) = \ln r_0 + \tan\theta_p(\phi - \phi_0). \quad (4)$$

We fit the spiral arms with equation (4) using a non-linear least-squares method,[4] using the Hα-bright regions as the input of the fitting process. The best-fitting line is the defined spiral arm ridge line, represented as the black solid line in Fig. 2. We present the phase diagram of only NGC 1566 in this paper for demonstration.

We aim to quantitatively trace the behaviour of star formation activities as stars and gas move in and out of the spiral arms. We adopt the parameter $\Delta\phi$, which quantifies the azimuthal distance to the nearest spiral arm at a constant galactocentric distance (Chen et al. 2024). Given a pixel T as the targeted pixel and pixel arm1, arm2,..., arm$N$ as pixels within the spiral regions at the same galactocentric distance, the $\Delta\phi$ is defined as,

$$\Delta\phi_T = -\min(|\phi_{\rm arm1} - \phi_T|, |\phi_{\rm arm2} - \phi_T|, ..., |\phi_{{\rm arm}N} - \phi_T|) \quad (5)$$

when pixel T is on the leading edge of the nearest spiral arm while

$$\Delta\phi_T = \min(|\phi_{\rm arm1} - \phi_T|, |\phi_{\rm arm2} - \phi_T|, ..., |\phi_{{\rm arm}N} - \phi_T|) \quad (6)$$

when pixel T is on the trailing edge of the nearest spiral arm. The $\Delta\phi$ map of NGC 1566 is presented in Fig. 3, overplotted with the spiral arm ridge lines.

We calculate the angular distance θ that stars will travel in 10 Myr, a typical life span of O-type stars, as:

$$t = \frac{2\pi R}{V_{\rm circ}},$$
$$\theta = \frac{10\ {\rm Myr}}{t} \times 360^\circ. \quad (7)$$

Here, $V_{\rm circ}$ is the circular velocity and R is the radial distance to the galaxy centre. Using a typical rotational velocity of 200 km s^{-1} (8 kpc to the centre of Milky Way; Honma, Nagayama & Sakai 2015), we get $\theta = 17^\circ$. For a conservative analysis, we classify spaxels with $|\Delta\phi| < 20^\circ$ as spiral arm regions, which will be applied to our statistic test (Section 4.2 and Fig. 8).

[4]We use the curve_fit module in PYTHON to carry out the fitting process.

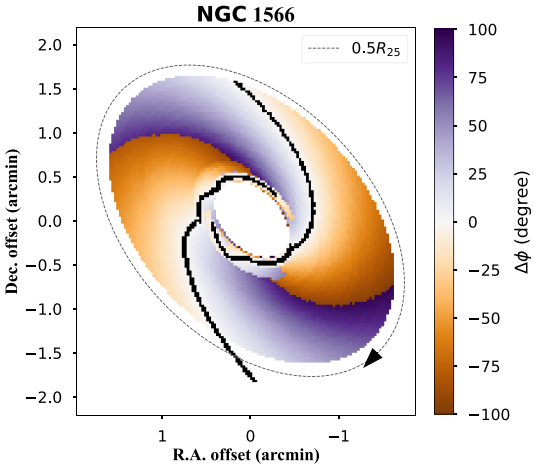

Figure 3. A measure of the angular azimuthal distance to the nearest spiral arm at a constant galactocentric distance ($\Delta\phi$), taking NGC 1566 as an example, overplotted with the spiral arm ridge lines. The solid ellipse shows the location of 0.5 R_{25}, with the circular flow indicated by the arrow. The orange spaxels on the leading edge are assigned negative values, while the spaxels on the trailing edge are given positive values, colour-coded as purple. The deeper colour the spaxel has, the further its azimuth is from the spiral arm.

3.4 Mapping the ISM: SFR and gas-phase metallicity

3.4.1 Mapping $\Sigma_{\rm SFR}$ *and* $\Delta\Sigma_{\rm SFR}$

The spatial distribution of star formation and gas-phase metallicities are critical components for understanding the physical evolution of spiral galaxies, including their ongoing star formation, star formation history, and mixing processes in the ISM (Maiolino & Mannucci 2019; Li et al. 2021; Garcia et al. 2023; Sharda et al. 2024). In this section, we introduce our method to map the SFR and the gas-phase metallicity, used to investigate the effects of the spiral arms on the SFR and metallicity distribution.

We measure the SFR by converting the extinction-corrected (i.e. intrinsic) Hα intensity to an SFR indicator. Stars with masses exceeding $\sim 10\ {\rm M}_\odot$ produce a detectable flux of ionizing photons

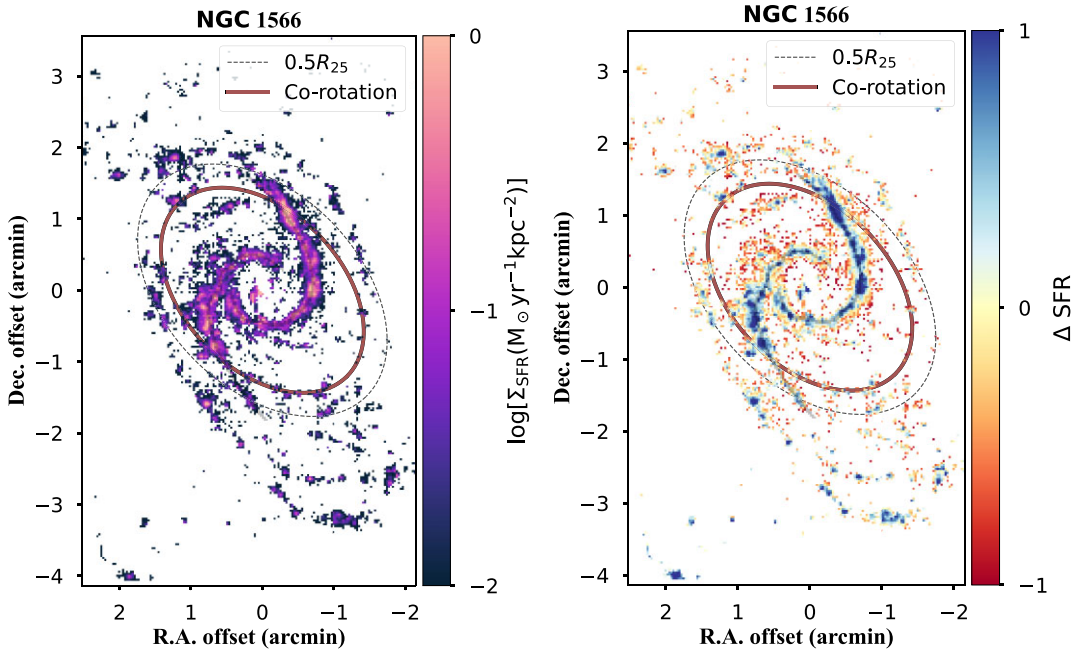

Figure 4. 2D maps of derived Σ_{SFR} and $\Delta\Sigma_{SFR}$ of NGC 1566 after SNR limit and spaxel selection based on BPT diagram, overplotted with the defined spiral arms from Section 3.3. The dashed ellipse marks the location of half R_{25} and the red ellipse denotes the CR reported in previous publications (see Section 5.3). Fig. A1 shows the SFR maps for the remaining galaxies in this work.

and have a short lifespan of $\lesssim$ 30 Myr (Calzetti 2013). The Hα nebular emission line is thus a direct tracer of the ionizing photons powered by young, massive stars. Following the SFR prescription in Kennicutt (1998), we measure the SFR as:

$$\mathrm{SFR}\left(\mathrm{M_\odot yr^{-1}}\right) = 7.9\times10^{-42}\times\ 4\pi D_\mathrm{L}^2 F_{\mathrm{H}\alpha}\left(\mathrm{erg\ s^{-1}\ cm^{-2}}\right), \quad (8)$$

where $F_{H\alpha}$ is the flux of Hα per spaxel and D_L is the luminosity distance in Table 1. We calculate the Σ_{SFR} as follows:

$$\Sigma_{\mathrm{SFR}}\left(\mathrm{M_\odot yr^{-1}kpc^{-2}}\right) = \frac{\mathrm{SFR}}{[D_\mathrm{A}(\mathrm{kpc})\times 1.65\,\mathrm{arcsec}/180^\circ\times\pi]^2}, \quad (9)$$

where 1.65 arcsec is the spaxel size of the TYPHOON data and D_A is the angular distance of the observed galaxy. The measured Σ_{SFR} map of NGC 1566 is shown in the left column of Fig. 4, with the remaining galaxies shown in Fig. A1.

We find higher Σ_{SFR} (bluer spaxels) predominantly concentrated in the central regions in most of our galaxies. To remove the radial dependence on the Σ_{SFR}, we subtract the radial gradient, represented by a piecewise linear function, from Σ_{SFR} to get the offset $\Delta\Sigma_{SFR}$ value, which indicates the azimuthal variation. The residual $\Delta\Sigma_{SFR}$ map of NGC 1365 is shown in the right column of Fig. 4, with the rest of the sample presented in Fig. A1.

We observe positive $\Delta\Sigma_{SFR}$ (i.e. higher Σ_{SFR}) along the spiral arm ridge lines of NGC 1566 which is expected from our definition of spiral arms (Section 3.3). This scenario is observed in all our galaxies (Fig. A1). With $\Delta\Sigma_{SFR}$ we can better compare both sides of the spiral arms, with generally negative $\Delta\Sigma_{SFR}$ in the leading edge (orange; $\Delta\phi < 0$) and positive $\Delta\Sigma_{SFR}$ in the trailing edge. The $\Delta\Sigma_{SFR}$ maps of other spiral galaxies can be found in Appendix A and we will further discuss the azimuthal variation in Section 4.1.

3.4.2 Mapping 12 + log(O/H) and Δlog(O/H)

Stars produce heavy metals during their lifetimes, which are subsequently released into the ISM upon their death, enhancing the metal content of the ISM for subsequent generations of stars. Consequently, gas-phase metallicity serves as a marker for preceding stellar generations, influenced by gas inflows, outflows, and depletion mechanisms. The spatial distribution of the gas-phase metallicity represents a snapshot in time of the production history and mixing processes. Deviations in the azimuthal direction of the metal distribution offer insights into the mixing process of metals with the surrounding ISM as both gas and stars orbit within the galactic potential. As oxygen is the most abundant metal in the gas-phase ISM, we measure the oxygen abundance through collisionally excited lines in the optical spectrum as an indicator of the gas-phase metallicity.

We adopt the N_2S_2–$N_2H\alpha$ diagnostic from Dopita et al. (2016, hereafter D16) to measure the gas-phase metallicity. The D16 diagnostic uses the Hα, [N II]λ6484 and [S II]$\lambda\lambda$6717,31 emission lines. All four emission lines above are well detected by the TYPHOON survey. With the inclusion of [S II]$\lambda\lambda$6717,31 doublet lines, the D16 diagnostic is subject to contamination from diffuse ionized gas (DIG; Zhang et al. 2017; Kumari et al. 2019; Shapley et al. 2019). Poetrodjojo et al. (2019) find that DIG has less impact on the calibrated metallicity at the resolution of the TYPHOON data, compared to Mapping Nearby Galaxies at APO (MaNGA) and SAMI. Appendix C further discusses the impacts of DIG with metallicity variation calculated by S-calibration (Pilyugin & Grebel 2016) diagnostic. Similarly, we find higher Δlog(O/H) in the trailing edge of NGC 1566, although the magnitude of the azimuthal variation (0.017 dex) is smaller than the one found in N_2S_2–$N_2H\alpha$ (0.037 dex).

We present the metallicity maps in the left panel of Fig. 5 (NGC 1566) and Fig. B1 for the remaining sample, overplotted with the defined spiral arms (Section 3.3). We find higher 12 + log(O/H) values in the central region (bluer spaxels) and lower 12 + log(O/H) measurements in the outskirts (redder spaxels) in all galaxies. The

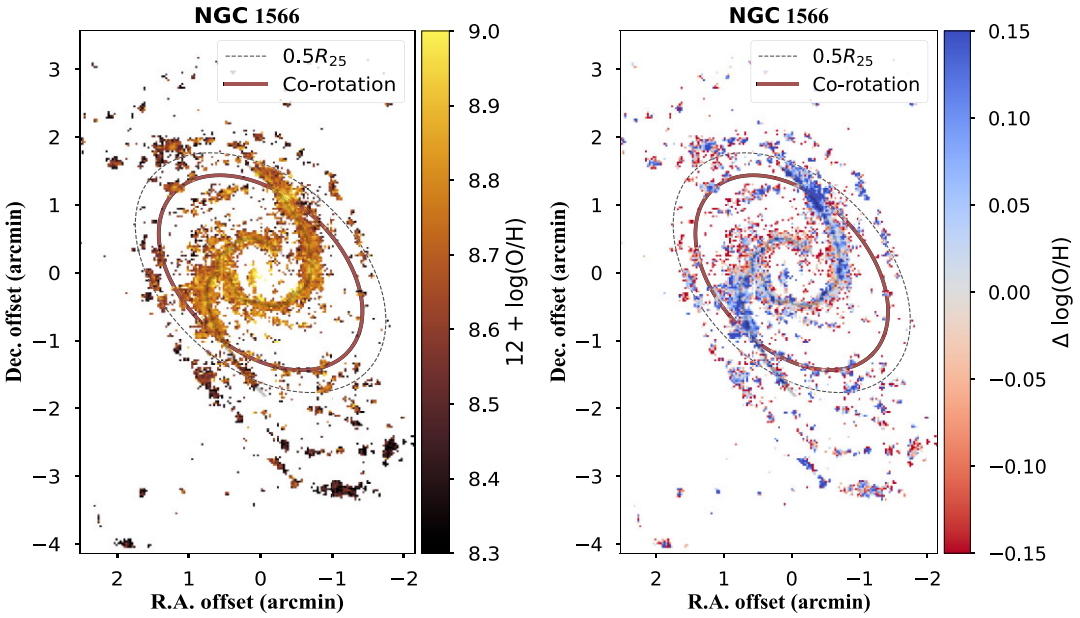

Figure 5. 2D maps of derived 12 + log(O/H) and Δlog(O/H) of NGC 1566, overplotted with the defined spiral arms from Section 3.3. The half R_{25} radius is shown as a dashed ellipse, while the CR is shown as a solid ellipse. The 12 + log(O/H) and Δlog(O/H) maps for the remaining sample are presented in Fig. B1.

negative radial metallicity gradient is indicative of inside–out galaxy formation (Tinsley & Larson 1978; Prantzos & Boissier 2000).

Similar to the methodology applied to $\Sigma_{\rm SFR}$, we derive the Δlog(O/H) value for each spaxel by subtracting the radial gradient, measured through the best fit of a piecewise linear function. The residual Δlog(O/H) maps are shown in the right panel of Fig. 5 and the second and fourth columns of Fig. B1. We observe generally positive Δlog(O/H) (blue pixels) along the spiral arms in all galaxies. To quantitatively compare the metallicity in the downstream versus upstream, we investigate the correlation between $\Delta\phi$ and Δlog(O/H) in the spiral galaxies in Section 4.2.

4 RESULTS

4.1 SFR

We examine the behaviour in SFR when moving into or out of the spiral arms by exploring the relation between $\Delta\Sigma_{\rm SFR}$ and $\Delta\phi$ (Fig. 6). $\Delta\Sigma_{\rm SFR}$ denotes a higher/lower SFR within the measured spaxel compared to those at the same galactocentric distance (Section 3.4) and $\Delta\phi$ quantifies the angular distance to the nearest spiral arm (Section 3.3). Gas flows from the trailing edge ($\Delta\phi > 0$) into the spiral arms, and then passes to the leading edge ($\Delta\phi < 0$). We measure the moving medians of each 20° (solid lines in Fig. 6), with blue shadow representing 25 per cent and 75 per cent quantiles. The fluctuation of $\Delta\Sigma_{\rm SFR}$ across different $\Delta\phi$ ranges from −1.5 to 1.5 dex.

In density wave theory, star formation may occur either (i) after gas clouds pass through density waves or (ii) as they approach density waves, resulting in various distributions of old stars, young stars, and gas (Pour-Imani et al. 2016). In scenario (i)/(ii), it is expected to observe a gaseous blue arm with young stars on the leading/trailing edge of a stellar arm inside the CR. Our work finds generally higher $\Delta\Sigma_{\rm SFR}$ on the trailing side ($\Delta\phi > 0$), with the highest $\Delta\Sigma_{\rm SFR}$ near the spiral arms and lower $\Delta\Sigma_{\rm SFR}$ on the leading edge ($\Delta\phi < 0$) of NGC 1365 and NGC 1566. This observation is consistent with density wave theory in the latter scenario, when star formation occurs as gas clouds approach the potential minimum (right spiral arms in fig. 1 of Pour-Imani et al. 2016). In NGC 2442, we find decreasing $\Delta\Sigma_{\rm SFR}$ in the trailing edge and increasing $\Delta\Sigma_{\rm SFR}$ in the leading edge ($\Delta\phi < 0$). Between $\Delta\phi$ of −20° and -50°, the trailing edge shows higher $\Delta\Sigma_{\rm SFR}$ than the corresponding leading edge, which is likely contributed by the interaction affecting this galaxy (further discussed in Section 5.4). In NGC 2835, NGC 2997, NGC 4536, NGC 5236, NGC 5643, and NGC 6744, we do not observe significant differences on either side of the spiral arms. This indicates that the $\Sigma_{\rm SFR}$ is comparable in these six galaxies and this finding aligns with the predicted symmetrical $\Sigma_{\rm SFR}$ from dynamic spiral theory. We do note that there is a large scatter in the $\Delta\Sigma_{\rm SFR}$–$\Delta\phi$ trend and it is possible that the non-detected offset in $\Sigma_{\rm SFR}$ could be due to noise obscuring the trend.

The varying motions of material inside and outside the CR might obscure and even eliminate the azimuthal offset. To address the potential obscuration of detecting azimuthal offset, separate analyses of $\Delta\phi$–$\Delta\Sigma_{\rm SFR}$ (Fig. 6) inside versus outside the CR or at various radial regions (if CR is unknown) are necessary. Among our sample, only three spiral galaxies have CR reported from the literature (see Section 5.3). To ensure consistency in our analyses, we examine the $\Delta\phi$–$\Delta\Sigma_{\rm SFR}$ trend at various radii for all galaxies, without using the reported CR for three of our samples. We divide each galaxy disc into two radial ranges, with an equal number of spaxels in each section.[5] The fluctuation of $\Delta\Sigma_{\rm SFR}$ along $\Delta\phi$ in the inner (outer) radial bin is presented as dotted (dashed) lines in Fig. 6. We observe the same $\Delta\Sigma_{\rm SFR}$–$\Delta\phi$ trend between the inner and outer regions in the eight of our spiral galaxies. NGC 4536 is the only spiral galaxy exhibiting an opposite $\Delta\Sigma_{\rm SFR}$ trend between the inner and outer regions, which

[5]The radial cut for each galaxy is: NGC 1365 – 10.98 kpc (0.37R_{25}), NGC 1566 – 8.80 kpc (0.41R_{25}), NGC 2442 – 10.35 kpc (0.61R_{25}), NGC 2835 – 5.81 kpc (0.58R_{25}), NGC 2997 – 7.95 kpc (0.54R_{25}), NGC 4536 – 7.43 kpc (0.50R_{25}), NGC 5236 – 4.66 kpc (0.38R_{25}), NGC 5643 – 4.76 kpc (0.42R_{25}), and NGC 6744 – 10.54 kpc (0.35R_{25}). This is also applied to the separation of inner and outer regions in Section 4.2 and Fig. 7.

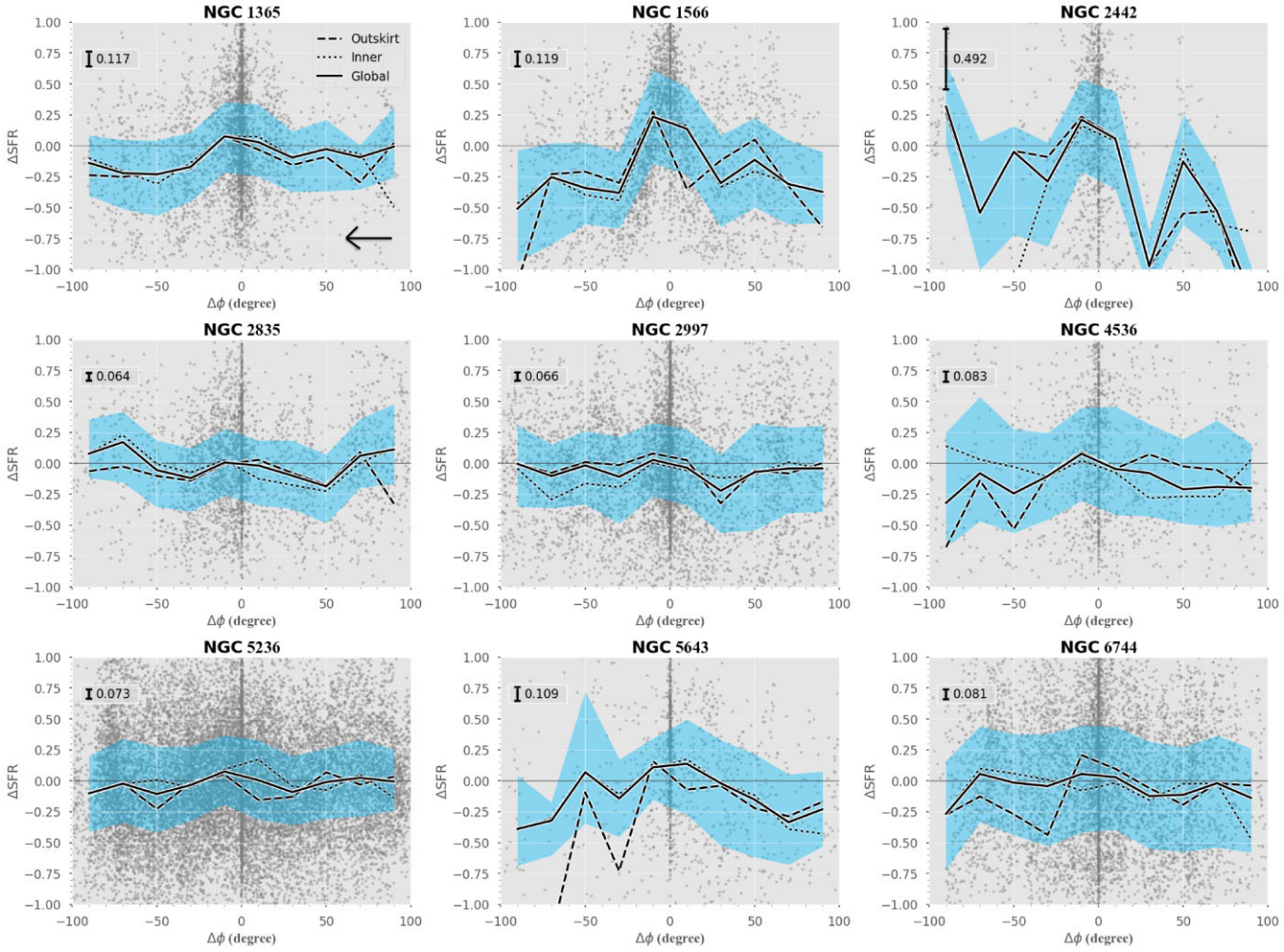

Figure 6. The fluctuation of $\Delta\Sigma_{\rm SFR}$ along $\Delta\phi$. The gas flows (shown as an arrow at the bottom right) from $\Delta\phi$ >0 (trailing) to $\Delta\phi$ <0 (leading). The solid black line marks the moving medians of each 20° $\Delta\phi$ bin, with 25 per cent and 75 per cent quartiles represented as the blue shadows. The average offset between $\Delta\Sigma_{\rm SFR}$ in the trailing and the leading edge is shown as a scale bar. We find subtly higher $\Delta\Sigma_{\rm SFR}$ in the trailing edge ($\Delta\phi$> 0) in NGC 1365 and NGC 1566. NGC 2442 shows higher $\Delta\Sigma_{\rm SFR}$ from −20° to −50°, compared to the trailing edge. We do not find a significant global azimuthal offset in $\Delta\Sigma_{\rm SFR}$ in the other six galaxy samples. We find an opposite trend of $\Delta\Sigma_{\rm SFR}$–$\Delta\phi$ in the inner region versus the outskirts only in NGC 4536, with large uncertainty and limited spaxels. We divide the galaxy disc into two regions: the inner region and the outskirts, with each region including half of the spaxels. We trace the fluctuation of $\Delta\Sigma_{\rm SFR}$ in the inner region using dotted lines and in the outskirts using dashed lines and eight out of nine galaxies (except for NGC 4536) show the same $\Delta\Sigma_{\rm SFR}$ trend in both inner and outer regions.

still fluctuates in between 25 per cent and 75 per cent quantiles (blue shadow).

4.2 12 + log(O/H)

As introduced in Introduction, spiral arms driven by density wave theory will lead to higher metallicity in the trailing edge than the leading edge, while dynamic spiral arms will not show azimuthal variations. Similar to $\Sigma_{\rm SFR}$ (Section 4.1), we will quantify the metallicity offsets on each side of the spiral arms.

Fig. 7 shows Δlog(O/H) versus $\Delta\phi$, showing the azimuthal fluctuation of the relative metal content once the global radial trend has been removed (Section 3.4.2). The spaxels with positive Δlog(O/H) represent regions of enriched gas, while spaxels with negative Δlog(O/H) values have less enriched gas. Similar to Section 4.1 with $\Sigma_{\rm SFR}$, we measure the moving medians of each 20° $\Delta\phi$ (solid black lines in Fig. 7). The 25 per cent and 75 per cent quantiles are shown as a blue-shaded region.

In NGC 1365, we observe increasing Δlog(O/H) from 100° to 20° and a drop of Δlog(O/H) from −20° to −50°. Both NGC 1365 and NGC 1566 show higher Δlog(O/H) in the trailing edge ($\Delta\phi$>0) than in the leading edge ($\Delta\phi$<0). This finding is consistent with the toy model in Ho et al. (2017), which predicts (i) a build-up of metal-rich gas in the trailing edge when the material rotates forward to the spiral arms; and (ii) a decrease in metallicity due to the mixing and diluting process when the material passes the spiral arms. We remind the readers that the model in Ho et al. (2017) assumes that gas overtakes the spiral patterns (i.e. inside the CR). In NGC 2442, we observe decreasing metallicity from $\Delta\phi\sim$ 70° to $\sim$ 20° and increasing metallicity at $\Delta\phi$ <−20 °. This does not align with either dynamic spiral theory or density wave theory. We attribute the azimuthal variation in NGC 2442 to the ongoing merging event (Section 5.4). In NGC 2835, NGC 2997, NGC 4536, NGC 5236, NGC 5643, and NGC 6744, we find no offset on both sides of the spiral arms, indicating no observed azimuthal variation in metallicity. This lack of azimuthal variation aligns with the prediction from the dynamic

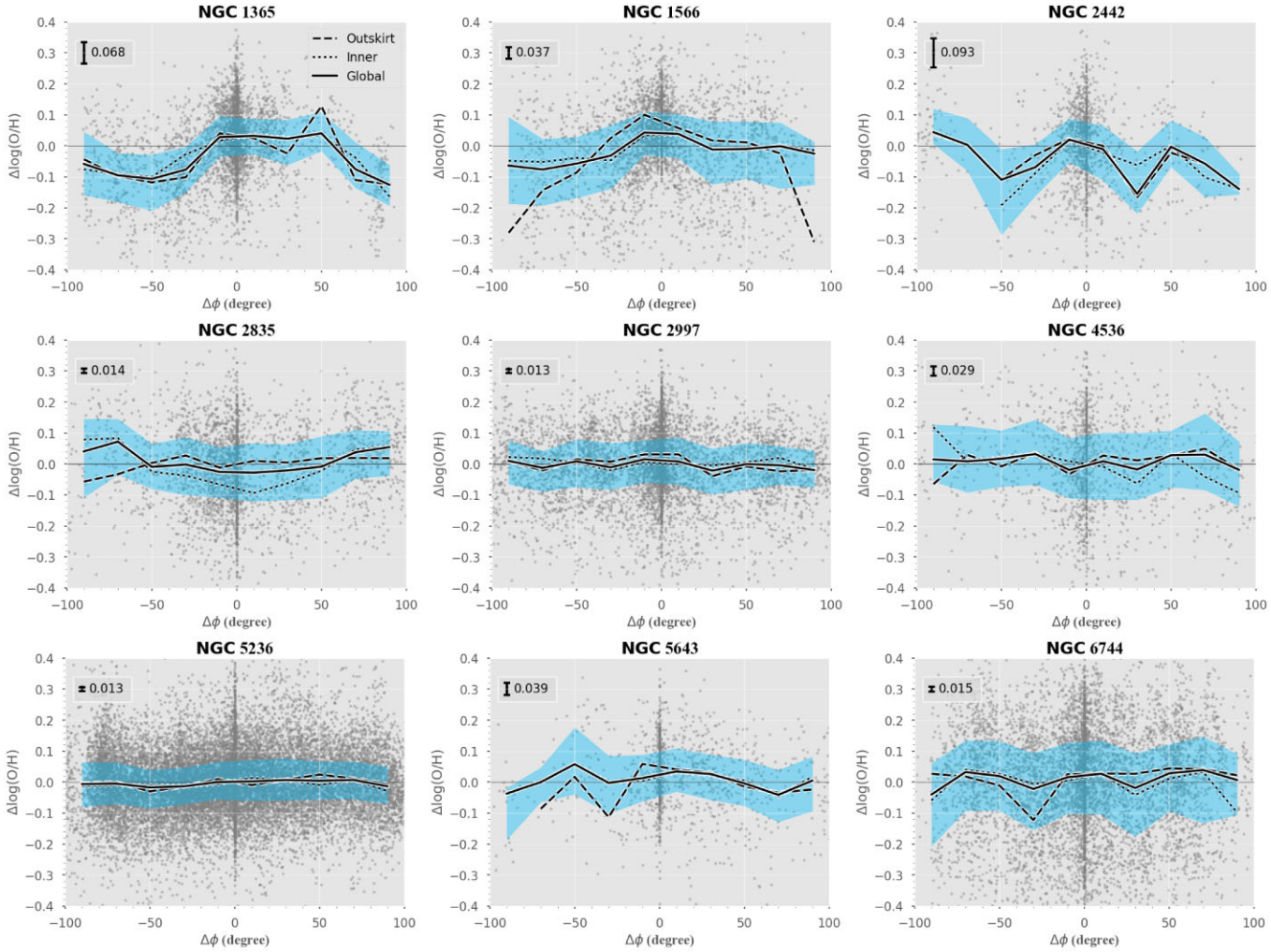

Figure 7. Similar to Fig. 6, but for Δlog(O/H). The gas flows (leftward) from 100° to 0° then towards −100°. The higher the Δlog(O/H) is, the more metal-rich the spaxel is, compared to other spaxels at the same galactocentric distance. We find significant offsets (> 0.1 dex) in the metallicity of NGC 1365, NGC 1566, and NGC 2442 ($\Delta\phi >$ 50). We find no significant azimuthal variation in the other six spiral galaxies. We do not find any opposite trend of Δlog(O/H)–$\Delta\phi$ in the inner region versus the outskirt. The Δlog(O/H) in the inner region of NGC 2835 is significantly different from the Δlog(O/H) in the outskirt, indicative of environmental effects in the outskirt.

spiral theory. However, the uncertainty of gas-phase metallicity and detection limit might also be attributed to the absent azimuthal variation. Further statistical analysis is carried out to test the reliability of the observed azimuthal variation in gas-phase metallicity (below).

The density wave theory predicts material to show opposite kinematics inside and outside the CR. The opposite motion leaves a caveat to interpreting the azimuthal variation without analysis of different radial ranges. Similar to Fig. 6, we divide the disc into two sections: inner region and outskirt, with an equal number of spaxels in each section. We present the azimuthal trend in Δlog(O/H) separately with dashed (outskirts) and dotted (inner) lines in Fig. 7. We do not observe a significant difference between the inner and outer regions in eight of our samples, except for NGC 2835. This divergence is evidence of the gas accretion from the circumgalactic medium of NGC 2835, which was detected in the flattened metallicity radial profile (Chen et al. 2023). The higher Δlog(O/H) near the spiral arms in the outskirts, compared to the inner region, supports the notion that spiral arms facilitate gas radial migration (Section 5.2).

To assess whether the metallicity on both sides of the spiral arms is drawn from the same parent distribution, we present histograms and cumulative distribution functions (CDFs) in Fig. 8, colour-coded by their location in their spiral arms: trailing (purple), leading (orange), and spiral arm (black) region. We conduct Kolmogorov–Smirnov test (KS) tests and Anderson–Darling (AD) tests, with p-values from both tests presented in Fig. 8. The D-value, representing the maximum absolute difference between the CDFs of metallicity on both sides, assesses whether metallicity distributions deviate from each other.

We test the detection limit of the statistical framework with the bootstrap resampling method. For each pixel in the galaxy, we calculate the error (σ_Z) through error propagation. In each bootstrapping trail, we generate a random metallicity map from a Gaussian distribution with a mean value of observed metallicity and standard deviation of σ_Z. After repeating the procedure 1000 times, we compute the mean values of D-values, p-values, and significance level, as well as the standard deviation. We summarize the D-values, KD/AD test results and their uncertainty in Table 2.

Fig. 8 shows that the trailing edge (purple) of NGC 1365 and NGC 1566 exhibit systematically higher metallicity than the leading

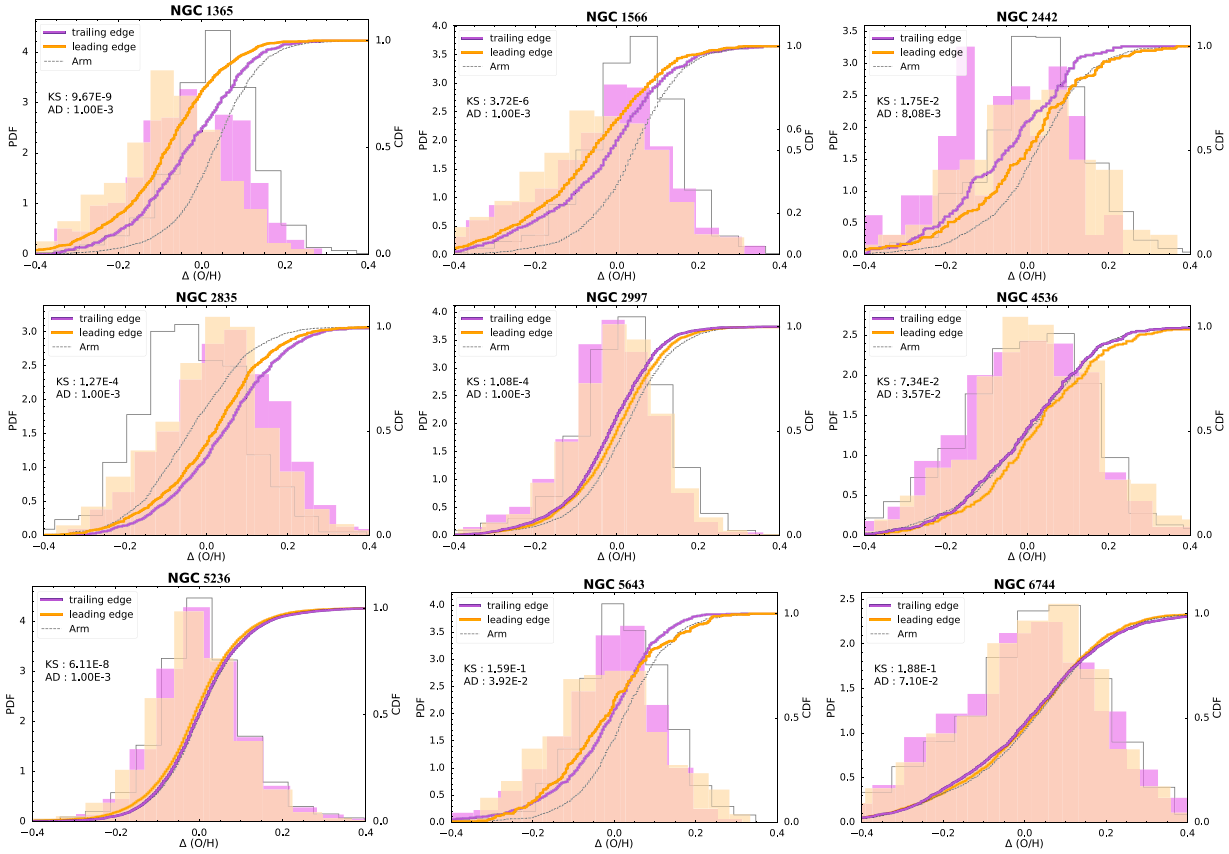

Figure 8. Histograms and CDF diagrams of $\Delta\log(O/H)$, colour-coded by their location to the spiral arms: purple marks the trailing edge of the spiral arms and orange marks the leading edge. We leave the gap within $-20^\circ < \Delta\phi < 20^\circ$ as the spiral arm region (black hollow histograms and black CDFs), which are not included in the leading/trailing edge regions. NGC 1365 and NGC 1566 show higher $\Delta\log(O/H)$ in the trailing edge (purple) than the leading edge (orange), while NGC 2442 presents higher $\Delta\log(O/H)$ in the leading edge. The other six galaxies show similar metallicity CDFs on both sides of the spiral arms.

Table 2. D-values, z-scores, and p-values from the KS tests, significance level from AD tests, and their uncertainty. The D-value indicates the largest vertical distance between the CDFs of the leading and trailing edge $\Delta\log(O/H)$. The z-scores quantify how significant the p-values (KS) are. A z-score of 1 corresponds to being 1 standard deviation away from the mean in a Gaussian distribution. The 1σ uncertainty in D-values, p-values, and significance level is the standard deviation of 1000 iterations of bootstrap resampling. We use asterisks to highlight p-values and significance levels below 0.05. Galaxies with both p-values and significance levels below 0.05 are highlighted in bold.

Galaxy	D-value	z-score	p-value (KS)	Significance level (AD)
NGC 1365	0.171 ± 0.013	4.70σ	$(1.33 \pm 5.41) \times 10^{-6}$*	1.00×10^{-3}*
NGC 1566	0.114 ± 0.015	2.92σ	$(1.18 \pm 3.27) \times 10^{-3}$*	$(1.51 \pm 2.51) \times 10^{-3}$*
NGC 2442	0.142 ± 0.025	1.25σ	$(1.05 \pm 1.12) \times 10^{-1}$	$(4.80 \pm 5.57) \times 10^{-2}$*
NGC 2835	0.084 ± 0.010	2.56σ	$(0.52 \pm 1.05) \times 10^{-2}$*	$(1.11 \pm 0.72) \times 10^{-3}$*
NGC 2997	0.075 ± 0.008	3.43σ	$(2.99 \pm 7.78) \times 10^{-4}$*	$(1.15 \pm 0.87) \times 10^{-3}$*
NGC 4536	0.070 ± 0.017	0.31σ	$(3.78 \pm 2.48) \times 10^{-1}$	$(9.82 \pm 8.18) \times 10^{-2}$
NGC 5236	0.043 ± 0.003	4.30σ	$(0.85 \pm 2.05) \times 10^{-5}$*	1.00×10^{-3}*
NGC 5643	0.073 ± 0.012	0.55σ	$(2.92 \pm 1.60) \times 10^{-1}$	$(1.30 \pm 0.67) \times 10^{-1}$
NGC 6744	0.030 ± 0.005	0.60σ	$(2.74 \pm 1.47) \times 10^{-1}$	$(8.49 \pm 5.33) \times 10^{-2}$

edge (orange), with a p-value[6] of 1×10^{-3} and $1.52\pm2.51 \times 10^{-3}$ from the AD test, respectively. The D-values of 0.171 and 0.114 also suggest the azimuthal variation in the metallicity of NGC 1365 and NGC 1566. Combined with the observed azimuthal variation seen in Σ_{SFR}(Fig. 6), this suggests that density wave theory drives the spiral features in both NGC 1365 and NGC 1566. In NGC 2442, the D-value of 0.142 and the p-value of $4.80\pm5.57 \times 10^{-2}$ from AD test indicate that the metallicity on both sides of the spiral arms is drawn from different parent distributions. However, NGC 2442 shows higher metallicity values in the leading edge (orange) instead of the trailing edge (purple), the opposite of what was observed in both NGC 1365 and NGC 1566. The kinematic and star-forming properties of NGC 2442 are indicative of what is expected from a typical interacting system shortly after the initial collision (Mihos & Bothun 1997). We thus attribute the opposite

[6]There is a lower limit of 1×10^{-3} for p-value from the AD test.

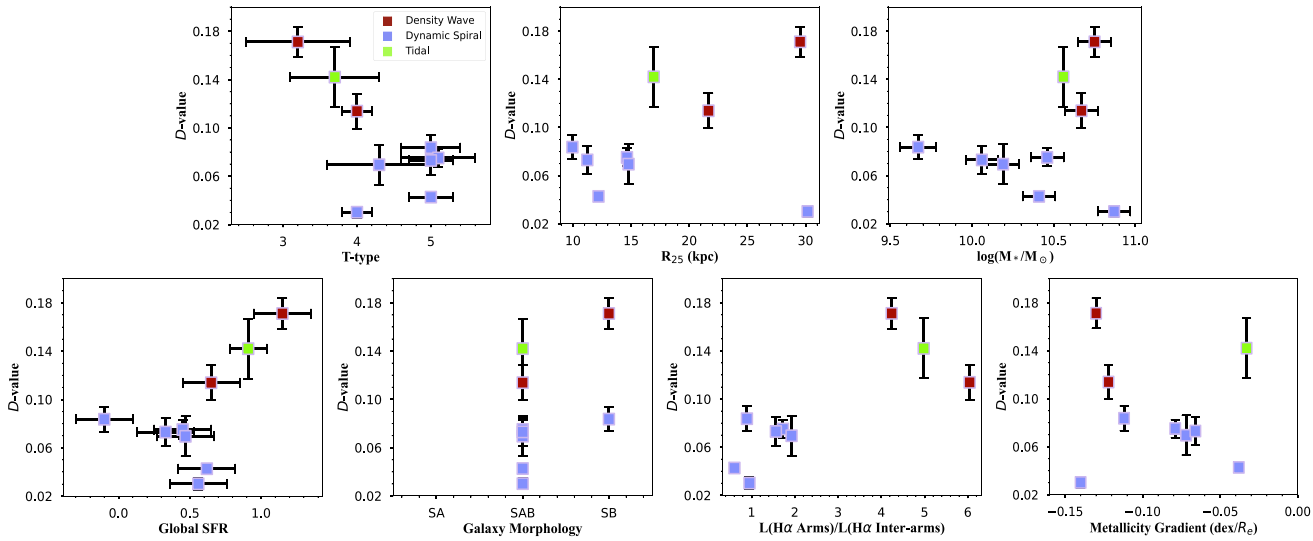

Figure 9. The relation between global properties and D-value drawn from metallicity CDFs (Fig. 8 and Table 2). The higher the D-value is, the greater the metallicity azimuthal variation is. All galaxies are colour-coded by their dominant mechanism that drives the origin of spiral arms. T-type is the numerical morphological type adopted from http://atlas.obs-hp.fr/hyperleda/, with 3 referring to Sb, 4 referring to Sbc, and 5 referring to Sc in the de Vaucouleurs (1959) morphological classification. We use R_{25} to represent the size of the galaxy disc, taken from Table 1. The stellar mass is the same as Table 1. The global SFR are taken from Leroy et al. (2019) [a]. The presence of a bar is taken from the morphological information in Table 1. The Hα luminosity ratios between the spiral arms ($|\Delta\phi| < 20°$) and the interarm regions describe the strength of spiral features. The radial gradient of metallicity is defined as the slope of the best linear fit on spaxels, in dex kpc^{-1} (further discussed in Section 5.2). *Note.*[a]The global SFR of NGC 2442 is taken from Pancoast et al. (2010) as it is not included in Leroy et al. (2019).

azimuthal variation trends present in metallicity to the ongoing merger.

In NGC 2835, NGC 2997, and NGC 5236, the AD test returns a p-value of $(1.11\pm0.72) \times 10^{-3}$, $(1.15\pm0.87) \times 10^{-3}$, and 1×10^{-3}, rejecting the hypothesis that the metallicities distributions are drawn from the same parent distribution. Interestingly, the metallicity offset between $\Delta\phi > 0$ and $\Delta\phi < 0$ is absent in Fig. 7 and absent in the CDFs with a D-value of 0.084 ± 0.010, 0.075 ± 0.008, and 0.043 ± 0.003, respectively. The small D-value in the metallicity of NGC 2835, NGC 2997, and NGC 5236 aligns with the prediction from dynamic spiral theory. The small p-value can be driven by (1) the tail of the distribution, as the mean values of the metallicity on both sides of the spiral arms are not distinguishable, and/or (2) the environmental effects such as gas accretion (Section 5.4) enhancing the metallicity asymmetry. We notice that NGC 2835 has surprisingly metal-poor spiral arms, compared to the interarm regions. This may result from the gas accretion from the circumgalactic medium (similar to NGC 2915; Werk et al. 2010).

The substantial scatter observed in both Σ_{SFR} and metallicity can obscure the detection of azimuthal offset, leading to a discrepancy between the absence of an azimuthal offset and the statistical tests of NGC 2835, NGC 2997, and NGC 5236. Previous studies on star clusters in NGC 5236 have reported: (i) a small fraction of higher Σ_{SFR} in the leading edge of one arm (Silva-Villa & Larsen 2012), and (ii) an azimuthal age gradient (Bialopetravičius & Narbutis 2020; Abdeen et al. 2022). These observational results, different from our work, may be attributed to the various analyses performed on star clusters and on spaxel levels. Measuring metallicity with less uncertainty and conducting deeper observations in fainter interarm regions could provide more evidence. In this paper, using the TYPHOON survey, we will maintain our discussion of the non-detected azimuthal variation in these three galaxies as a preference for dynamic spiral theory.

NGC 4536, NGC 5643, and NGC 6744 show highly similar metallicity CDF between the leading edge and trailing edge, with a p-value larger than 0.05. These symmetrical distributions in metallicity show a preference for the dynamic spiral theory when explaining the formation of spiral features in these five galaxies. We test our detection limit with 1000 times bootstrapping within the metallicity measurement uncertainty. The lower than 0.05 p-values, even with the uncertainty, suggest the absent azimuthal variation in NGC 4536, NGC 5643, and NGC 6744 are not obscured by the detection limit.

5 DISCUSSION

5.1 Global galaxy properties and azimuthal variations

In this work, three of our nine galaxies (NGC 1365, NGC 1566, and NGC 2442) show statistically significant azimuthal variation in metallicity. Similarly, Kreckel et al. (2019) found subtle azimuthal variation in half of their galaxy samples but not always associated with the spiral features. It is important to study the correlation between the global properties of spiral galaxies and the presence of azimuthal variation in the gas-phase metallicity. This will bring us hints on which type of spiral galaxies tend to exhibit observable azimuthal variation in metallicity.

In Fig. 9, we show the correlation between D-values calculated from metallicity CDFs (Fig. 8) and global galaxy properties, including the tightness of spiral arms (T-type), disc size, stellar mass, global SFR, the presence of a bar, amplitude of spiral arms and metallicity gradient. The points are colour-coded by their dominant mechanism that drives the spiral features (Section 4.2 and further discussed in Section 5.4). In Fig. 9, we find that more open-armed galaxies (large T-type) tend to have low D-values while less open-armed galaxies (small T-type) exhibit large D-values. There is a weak but positive correlation between R_{25} and D-values, with one outlier

Table 3. This table shows the metallicity gradient fitted by a single and piecewise linear function, with both the inner and outer gradients listed sequentially. The break radius of the piecewise fits is listed in the last row. All of the observed spiral galaxies show a negative metallicity gradient, consistent with an inside–out galaxy formation. The galaxies showing a flattening metallicity gradient truncated outside 2 kpc are in bold.

Galaxy	NGC 1365	NGC 1566	NGC 2442	NGC 2835	NGC 2997
Single linear (dex/R_e)	−0.136	−0.144	−0.014	−0.119	−0.077
Piecewise fits (dex/R_e)	**−0.664, −0.093**	−0.118, −0.156	**−0.816, −0.00**	**−0.152, −0.078**	−0.037, −0.097
Break radius (kpc)	4.82	8.00	1.93	6.00	6.73
Galaxy	NGC 4536	NGC 5236	NGC 5643	NGC 6744	
Single linear (dex/R_e)	−0.086	−0.038	−0.066	−0.132	
Piecewise fits (dex/R_e)	**−0.281, −0.068**	**−0.075, 0.038**	**−0.262, −0.061**	0.030, −0.160	
Break radius (kpc)	2.77	5.37	1.85	7.65	

galaxy, NGC 6744. Our finding suggests that more extended galaxies tend to have stronger azimuthal variation in metallicity compared to compact galaxies. We present the strength of spiral arms using the Hα luminosity ratio between the spiral arm regions ($|\Delta\phi| < 20°$) and the interarm regions. Our galaxies show larger D-values with stronger spiral arms, which suggests that galaxies with more pronounced spiral arms tend to have greater metallicity offset on both sides of spiral arms. Similarly, Sánchez-Menguiano et al. (2020) find the metallicity difference of arm versus interarm is larger ($\sim$ 0.015 dex) in grand design than in flocculent galaxies. More studies on nearby galaxies can fill up the gap between strong spiral arms ($\frac{L_{\rm arm}}{L_{\rm interarm}} > 4$) and weak spiral arms ($\frac{L_{\rm arm}}{L_{\rm interarm}} < 3$) and provide more constraints. The galaxies in our sample do not show a clear correlation between the D-values and the stellar mass, global SFR, and the presence of a bar. A larger sample of spiral galaxies will improve the study of the correlation between azimuthal variations and global galaxy properties.

5.2 Impacts of radial streams and radial migration

Previous simulations have discussed the impacts of radial streams and radial migration on azimuthal variations of gas and stars (e.g. Sellwood & Binney 2002; Grand, Kawata & Cropper 2015; Grand & Kawata 2016; Orr et al. 2023). Radial stellar migration can move metal-rich star particles outward along the trailing edge, while bringing metal-poor star particles inward along the leading edge (e.g. Grand et al. 2016). Radial gas streams can lead to azimuthal variations of gas-phase metallicity distribution, with metal-rich gas concentrated in the trailing side of the stellar spiral arm (e.g. Khoperskov et al. 2023). Sánchez-Menguiano et al. (2016) found azimuthal variations of gas metallicity in NGC 6754, where large-scale gas radial migration is also detected. Radial migration is expected to be stronger in a bar-spiral coupled system (Minchev & Famaey 2010). Given the varying bar strength in our sample, ranging from strong to weak, it is important to discuss the impacts of radial migration in our study of azimuthal variation.

Measuring and modelling the velocity field to investigate the radial gas migration is out of the scope of this paper. Instead, we adopt the radial metallicity gradient as an indicator for radial gas migration. We measure the radial metallicity gradient with a single linear function, listed in Table 3, each showing a negative metallicity gradient. The negative metallicity gradients are consistent with an inside–out galaxy formation. Seven of our galaxies (except for NGC 2442 and NGC 5236) have comparable radial metallicity gradients with those reported in previous studies, such as the the Calar Alto Legacy Integral Field Area survey CALIFA survey (−0.1 dex/R_e; Sánchez et al. 2015a), and the MaNGA survey (−0.14 dex/R_e; Belfiore et al. 2017). The shallow metallicity gradients in NGC 2442 and NGC 5236 could be indicative of large-scale radial gas flows dispersing and flattening the metal distribution. A large sample of spiral galaxies is needed to establish a stronger relation between metallicity gradients and azimuthal variations.

The final panel in Fig. 9 compares the radial metallicity gradients of our sample and their D-values from metallicity CDF in the leading and trailing edge. We cannot draw a conclusive correlation between the metallicity radial gradient and D-values. In the shallow radial gradient regime ($\lesssim$−0.05dex/R_e), where strong and large-scale radial gas flows are expected to exist, we find both galaxies with high (NGC 2442) and low (NGC 5236) D-values. This result suggests that large-scale radial gas flow does not necessarily lead to strong azimuthal offset in metallicity.

A truncated metallicity radial gradient, especially a flattening gradient in the outer parts, is possibly a phenomenon driven by radial gas mixing (Minchev et al. 2011; Sánchez-Menguiano et al. 2018; Garcia et al. 2023; Kewley et al. submitted). We summarize the best fit of a piecewise linear function on gas-phase metallicity (Section 3.4.2) in Table 3. We find a shallow-steep metallicity radial profile in NGC 1566, NGC 2997, and NGC 6744. In NGC 1365, NGC 2442, NGC 2835, NGC 4536, NGC 5236, and NGC 5643, we observe a flattening of the metallicity radial gradient, that is, the outer gradient is less than half as steep as the inner gradient. This phenomenon could be indicative of radial gas migration outside the break radius (Minchev et al. 2011) and/or satellite accretion (Qu et al. 2011). Among the six spiral galaxies with a flattening metallicity radial gradient, an azimuthal offset is observed in NGC 1365 and NGC 2442. In NGC 1365, we cannot distinguish the dominant mechanisms driving the azimuthal variation, with the potential involvement of both density wave theory and radial gas motion. The merging event in NGC 2442 can be attributed to the strong radial gas mixing and meanwhile azimuthal variations in metallicity.

5.3 Inside and outside the corotation radius

The asymmetric distributions of $\Sigma_{\rm SFR}$ and gas-phase metallicity in NGC 1365 and NGC 1566 (Sections 4.1 and 4.2) suggest that the density wave theory explains the origin of their spiral features. According to the density wave theory, the material surpasses the spiral density wave inside the CR while lagging behind the density wave outside the CR. A simulation by Spitoni et al. (2019) shows that the density perturbation of a disc model can result in stronger oxygen abundance fluctuations in the outer region compared to the inner regions of a galaxy. When an analytic spiral arm[7] is included in the simulation, and the fluctuations near the corotation resonance

[7]Analytic spiral arms show regular gravitational perturbation with a fixed pattern speed. The surface arm density can be described by the radial distance and the azimuth.

Table 4. The CR of NGC 1365, NGC 1566, and NGC 5236 reported in previous publications. We take the mean values as the CR in the analysis in this work.

Galaxy	CR (kpc)	References
NGC 1365	13.8	Lindblad, Lindblad & Athanassoula (1996); Elmegreen, Galliano & Alloin (2009)
NGC 1566	8.8	Scarano & Lépine (2013); Abdeen et al. (2020)
NGC 5236	8.5	Scarano & Lépine (2013); Abdeen et al. (2020)

are enhanced. To further compare the observations and simulations, it is essential to assess the behaviour of ISM inside/outside the CR.

Although it is challenging to measure the CR, astronomers have devoted numerous efforts to measuring the CR of nearby spiral galaxies with various methods. Three of our observed spiral galaxies (NGC 1365, NGC 1566, and NGC 5236) have their CR reported in previous works and collected in Table 4.

With the location of CR, we divide the spiral galaxies into three sections: inside the CR, near the CR, and outside the CR. We exclude NGC 5236 in the following discussion since the CR of NGC 5236 is more than 3 kpc beyond the observed optical disc in the TYPHOON survey. Fig. 10 compares the behaviour of metallicities at different azimuths and radii, indicated by colours. The azimuth starts from the position angle in Table 1 and increases counterclockwise to 360°.

We observe the smallest azimuthal fluctuation (0.13 dex for NGC 1365 and 0.07 dex for NGC 1566) of metallicity in the inner region (grey line in Fig. 10), in agreement with the observations of NGC 6754 (fig. 7 in Sánchez et al. 2015b). In NGC 1365, we find that the fluctuations in metallicity with azimuth are comparable when near (0.24 dex) and outside the CR (0.25 dex), which is significantly larger than those within the CR. As an analytic spiral arm (Spitoni et al. 2019) predicts the largest metallicity fluctuation near the CR, our observation indicates the presence of a density perturbation in NGC 1365, resulting in a greater metallicity fluctuation beyond the CR. Additionally, we notice that the $\Delta\log(O/H)$ offset between the leading and trailing edge (Fig. 7) is slightly larger in the outskirts ($R > 10.98$ kpc) than in the inner region ($R < 10.98$ kpc). The absent opposing behaviour inside versus outside the CR (13.8 kpc) does not align with the prediction of density wave theory. However, there is a large uncertainty in the detection of CR. In Ho et al. (2017), they adopt a larger CR where all observed spaxels in the TYPHOON field are within the CR. In this case, the consistent $\Delta\log(O/H)$–$\Delta\phi$ trend at different radii (dashed and dotted lines in Fig. 7) aligns with the prediction of density wave theory within the CR.

In NGC 1566, the metallicity shows the highest fluctuation near the CR (0.21 dex) when compared with the metallicity fluctuation outside the CR (0.12 dex) and within the CR (0.07 dex). This is in line with the predictions from Spitoni et al. (2019), indicating that the spiral arms in NGC 1566 are also analytic.

Inside the CR, the metallicity fluctuation can be decreased or wiped out by the rotation of material, due to the decreased travel distance between spiral arms. We calculate the time-scale required to travel between spiral arms, in order to assess the reliability of the small-scale metallicity fluctuations we measured. We calculate the angular distance that stars will travel in 10 Myr, a typical life span of O-type stars, using equation (3.3). The $V_{\rm circ}$ of NGC 1365 is ~ 300 km s^{-1} at ~ 100 arcsec (~ 8 kpc; Jorsater & van Moorsel 1995), while NGC 1566 has a $V_{\rm circ}$ of ~ 180 km s^{-1} at 6 kpc (Elagali et al. 2019). Following equation (7), we find the rotation angle within 10 Myr is $\lesssim 20°$ inside the CR for both NGC 1365 and NGC 1566, which is smaller than the azimuthal distance between two spiral arms. Considering the flattening of the rotation curve, we find that the rotation angle is $>20°$ outside the CR of NGC 1365 and NGC 1566. Hence, the fluctuation of metallicity cannot be wiped out by the rotational motion of the material, even inside the CR. Therefore, the observed smaller metallicity fluctuation within the CR can be considered reliable and meaningful.

5.4 Dominant mechanisms driving spiral features of each galaxy

In this section, we discuss the underlying mechanisms driving the formation of spiral arms in our galaxies, taking into account the distributions of $\Sigma_{\rm SFR}$, $12 + \log(O/H)$ from the TYPHOON survey, as well as the environmental factors reported in previous works.

NGC 1365 is a grand-design spiral galaxy in the Fornax cluster. The small fragments near the two prominent spiral arms infer that NGC 1365 has undergone tidal interaction. In this work, we find slightly higher $\Sigma_{\rm SFR}$ (Section 4.1) and generally higher metallicity (Section 4.2) in the trailing edge ($\Delta\phi > 0$) of the spiral arms. These scenarios are supportive evidence for density wave spiral arms. However, the radial gas motion, indicated by the flattening metallicity gradient (Section 5.2), can also result in the azimuthal variation in $\Sigma_{\rm SFR}$ and $\Delta\log(O/H)$. We notice a comparable fluctuation in

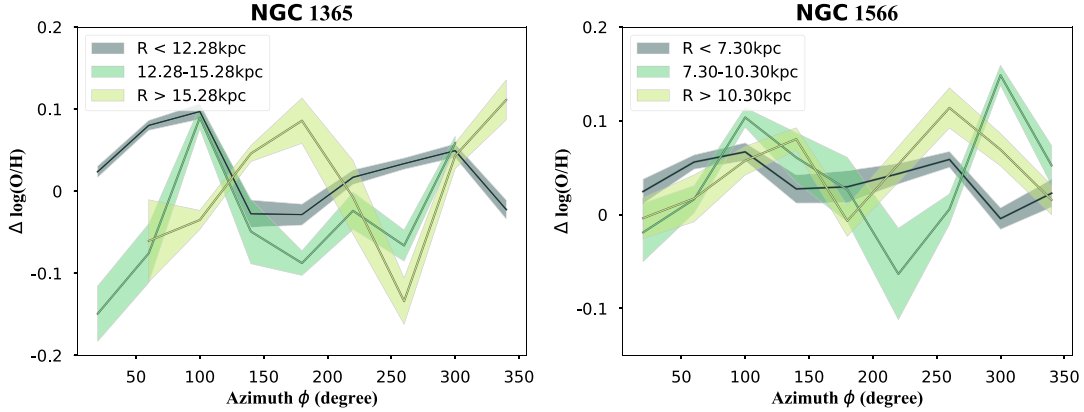

Figure 10. Residual of gas-phase metallicity as a function of azimuth inside the CR (grey), near the CR (green), and beyond the CR (lime). The azimuth starts from the position angle (Table 1) and increases counterclockwise. We apply bootstrapping for 500 iterations and show the medians with 1σ uncertainty in the figure. The shadow of the lines indicates 1σ of the medians.

metallicity near (0.24 dex) and beyond (0.25 dex) the CR, which is twice as pronounced as the fluctuation within the CR (13.8 kpc). This observation supports the influence of tidal interactions, by comparison with the simulated model in Spitoni et al. (2019).

According to the asymmetric H I distribution (Elagali et al. 2019), NGC 1566 is possibly experiencing ram-pressure interaction with the intergalactic medium in the Dorado cluster. Slater et al. (2019) report the strong outflows observed in ionized and molecular gas in the central kpc along the bar and the spiral arms. Our observations show generally higher $\Sigma_{\rm SFR}$ and higher metallicity in the trailing edge ($\Delta\phi > 0$) of the spiral arms. This evidence supports that the spiral arms in NGC 1566 follow the density wave theory. The strongest metallicity fluctuations near the CR (Fig. 10) are consistent with the simulated galaxy with an analytic spiral arm.

NGC 2442 is a system undergoing a merger (Mihos & Bothun 1997; Pancoast et al. 2010) and the south and north spiral arms are distorted fragments from the same galaxy (NGC 2442 and NGC 2443, respectively). Our observations find significantly lower $\Sigma_{\rm SFR}$ and lower metallicity in the trailing edge ($\Delta\phi > 0$) of the spiral arms, which is unexpected by either density wave theory or dynamic spiral theory. The spiral features in NGC 2442 are dominated by the gravity perturbation from the ongoing tidal interactions and the induced strong gas radial migration (Section 5.2).

NGC 2835 is a multi-armed spiral galaxy in a small galaxy group (Anand et al. 2021), with ESO 497 − 035 and ESO 565 − 001. The flattened metallicity radial profile, happening at $\sim$ 7 kpc, indicates the gas accretion from the circumgalactic medium to the outskirts of the galaxy (Chen et al. 2023; Garcia et al. 2023). We observe negligible offset in $\Sigma_{\rm SFR}$ and 12 + log(O/H), given the scatters of the spaxels. The *D*-value is not significant while the KS and AD tests suggest the metallicity on both sides of the spiral arms are drawn from different distributions. This result suggests the spiral arms in NGC 2835 follow the dynamical spiral theory, potentially under the density perturbation from the accreted gas, flattening the metallicity gradient in the outskirts (Table 3).

NGC 2997 belongs to a loose galaxy group and has undergone tidal interaction according to the anomalous H I distribution (Hess et al. 2009). We observe generally no offset between both sides of the spiral arms, either in $\Sigma_{\rm SFR}$ or 12 + log(O/H). This suggests that tidal interaction does not necessarily lead to azimuthal variation in $\Sigma_{\rm SFR}$ and 12 + log(O/H). The tidal-induced spiral arms in NGC 2997 behave similarly to dynamic spiral arms, instead of density-wave-like structures.

NGC 4536 is located in the Virgo cluster without evident hints of tidal interaction. The only kinematic perturbation is the bar-induced inflows observed in the H I map (Davies, Sugai & Ward 1997). We observe slightly lower $\Sigma_{\rm SFR}$ and lower metallicity in the trailing edge ($\Delta\phi > 0$). However, the CDF diagram shows no offset between the downstream and upstream. The *p*-value (3.78×10^{-1}) from the KS test suggests that the metallicity on both sides of the spiral arms is drawn from the same parent distribution. Therefore, we conclude that the current TYPHOON data suggest NGC 4536 follows the dynamic spiral theory, with insufficient spaxels to discern the azimuthal variations.

NGC 5236 (M83) is the largest member in its galaxy group. There is a large optically detected tidal stream to the north of M83 (Malin & Hadley 1997; Pohlen et al. 2004; Jarrett et al. 2013), tracing the disruption of a dwarf galaxy in the strong gravitational field of M83. The penetrating gas stream may be attributed to the flattening metallicity gradient beyond 5.37 kpc (Table 3). Unlike studies on star clusters (Silva-Villa & Larsen 2012; Bialopetravičius & Narbutis 2020; Abdeen et al. 2022) and full-spectral fitting (Sextl et al. in preparation), we observe no significant offset in either $\Sigma_{\rm SFR}$ or 12 + log(O/H) between the two sides of the spiral arms. Our observations do not support the density wave theory but rather show a preference for the dynamic spiral theory.

As a type-II Seyfert galaxy (Simpson et al. 1997), NGC 5643 is in a small galaxy group with NGC 5530 and has a dwarf satellite ESO 273 − 014. After excluding the hard component contaminated spaxels, we find slightly higher $\Sigma_{\rm SFR}$ in part of the trailing edge ($\Delta\phi > 70$) and lower metallicity in the trailing edge ($\Delta\phi > 0$). However, the CDF diagram shows no offset and the KS test agrees that the metallicity in the downstream and upstream is drawn from the same distribution. This finding implies that no statistical offset is found in NGC 5643 based on the TYPHOON data, due to the limited spaxel in the interarm regions (especially $\Delta\phi < 0$). We agree that NGC 5643 follows the dynamic spiral theory, instead of the density wave theory.

NGC 6744 is a spiral galaxy in the Virgo supercluster. The H I in NGC 6744 is possibly connected to a companion galaxy, ESO 104 − g44 (Ryder, Walsh & Malin 1999). We observe a slightly increasing trend in $\Sigma_{\rm SFR}$ and Δlog(O/H) when crossing the spiral arms from the trailing edge ($\Delta\phi > 0$) to the leading edge ($\Delta\phi < 0$). However, the difference in Δlog(O/H) is not statistically evident in the CDF and the KS test. Our findings suggest that under environmental influences, NGC 6744 shows a preference for dynamic spiral theory with absent azimuthal variation.

6 SUMMARY

We map the 2D ISM properties, $\Sigma_{\rm SFR}$, and gas-phase metallicity, of nine spiral galaxies in the TYPHOON survey. The 3D data set and wide FoV, covering most of the star-forming disc of each galaxy, allows us to constrain spaxel-by-spaxel fluctuations in ISM properties as a function of azimuthal distance from the spiral arms in each galaxy. These azimuthal distributions constrain the dominant mechanism driving the spiral arms, which can assess the density wave theory.

Considering the azimuthal ISM distribution observed in TYPHOON and the environment reported in previous works (Section 5.4), we discuss the dominant theory/theories that drive the spiral features in our samples. We find higher $\Sigma_{\rm SFR}$ (Fig. 6) and higher gas-phase metallicity (Fig. 7) in the trailing edge of NGC 1365 and NGC 1566, which is in line with expectations from density wave theory driving the observed spiral features in these two galaxies. Additionally, the higher $\Sigma_{\rm SFR}$ in the trailing edge indicates that star formation occurs when gas clouds approach the density wave (right spiral arms in fig. 1 of Pour-Imani et al. 2016) in NGC 1365 and NGC 1566. The interacting galaxy, NGC 2442, presents significantly lower metallicity in part of the trailing edge ($\Delta\phi < 50$), opposite to the expectation of density wave theory, which can be attributed to the ongoing merging event. We do not observe statistically significant offset in the interarm regions of the remaining six galaxies, in line with the prediction of dynamic spiral theory.

We investigate the global properties of galaxies and the *D*-values from metallicity CDFs, indicating the significance of azimuthal variations. We find that more prominent spiral arms, more open-armed and more extended galaxies tend to show stronger azimuthal variations in metallicity.

We collect the CR from the earlier works and compare the azimuthal variation in metallicity within and beyond the CR (Section 5.3). In NGC 1365, we find the smallest metallicity fluctuation inside the CR and comparable fluctuation near and outside the CR. This is consistent with a simulated density wave spiral galaxy under gravity perturbation in the outer region (Spitoni et al. 2019). In NGC 1566,

we observe the greatest metallicity fluctuation near the CR, aligning with an analytic spiral arm where gravity perturbation is regular.

Our work highlights the importance of azimuthal variations in ISM, which constrain the dominant mechanism driving spiral features. Different theories, including the density wave theory, dynamic spiral theory, and tidal interactions, can explain the formation of spiral arms in various galaxies in the local Universe. Despite our handful of galaxy samples, we observe a positive relation between azimuthal metallicity variation and T-type, galaxy size, and arm strength. A larger sample of observations and a comparison between simulations and observations are essential for more constraints on the dominant mechanism driving spiral arms.

ACKNOWLEDGEMENTS

We gratefully acknowledge the anonymous referee for their highly constructive and valuable comments, which have significantly improved the scientific quality of this paper. This paper includes data obtained with the du Pont Telescope at the Las Campanas Observatory, Chile, as part of the TYPHOON programme, which has been obtaining optical data cubes for the largest angular-sized galaxies in the Southern hemisphere. We thank past and present Directors of The Observatories and the numerous time assignment committees for their generous and unfailing support of this long-term programme.

This research has made use of NASA's Astrophysics Data System Bibliographic Services (ADS). This research made use of ASTROPY,[8] a community-developed core PYTHON package for Astronomy (Astropy Collaboration 2013, 2018). This research has made use of the NASA/IPAC Extragalactic Database (NED) which is operated by the Jet Propulsion Laboratory, California Institute of Technology, under contract with NASA.

KG is supported by the Australian Research Council through the Discovery Early Career Researcher Award (DECRA) Fellowship DE220100766 funded by the Australian Government. KG is supported by the Australian Research Council Centre of Excellence for All Sky Astrophysics in 3 Dimensions (ASTRO 3D), through project no. CE170100013.

ES acknowledges support by the Munich Excellence Cluster Origins funded by the Deutsche Forschungsgemeinschaft (DFG, German Research Foundation) under Germany's Excellence Strategy EXC-2094 390783311.

DATA AVAILABILITY

The TYPHOON team is planning for a public data release on Data Central[9] once the observation is complete. The TYPHOON data and the code in this article will be shared on reasonable request to the corresponding author.

REFERENCES

Abdeen S., Kennefick D., Kennefick J., Miller R., Shields D. W., Monson E. B., Davis B. L., 2020, MNRAS, 496, 1610
Abdeen S. et al., 2022, MNRAS, 512, 366
Anand G. S. et al., 2021, MNRAS, 501, 3621
Astropy Collaboration, 2013, A&A, 558, A33
Astropy Collaboration, 2018, AJ, 156, 123
Athanassoula E., 1992, MNRAS, 259, 345
Athanassoula E., Romero-Gómez M., Bosma A., Masdemont J. J., 2010, MNRAS, 407, 1433
Baldwin J. A., Phillips M. M., Terlevich R., 1981, PASP, 93, 5
Belfiore F. et al., 2017, MNRAS, 469, 151
Bertin G., Lin C. C., 1996, Spiral Structure in Galaxies a Density Wave Theory. MIT Press, Cambridge, MA
Bialopetravičius J., Narbutis D., 2020, AJ, 160, 264
Binney J., Tremaine S., 1987, Galactic Dynamics. Princeton Univ. Press, Princeton, NJ
Binney J., Tremaine S., 2008, Galactic Dynamics, 2nd edn. Princeton Univ. Press, Princeton, NJ
Brinchmann J., Charlot S., White S. D. M., Tremonti C., Kauffmann G., Heckman T., Brinkmann J., 2004, MNRAS, 351, 1151
Calzetti D., 2001, PASP, 113, 1449
Calzetti D., 2013, in Falcón-Barroso J., Knapen J. H., eds, Secular Evolution of Galaxies. Cambridge Univ. Press, Cambridge, UK, p. 419
Cappellari M., 2017, MNRAS, 466, 798
Cappellari M., Emsellem E., 2004, PASP, 116, 138
Chen Q.-H., Grasha K., Battisti A. J., Kewley L. J., Madore B. F., Seibert M., Rich J. A., Beaton R. L., 2023, MNRAS, 519, 4801
Chen Q.-H. et al., 2024, MNRAS, 527, 2991
Choi Y., Dalcanton J. J., Williams B. F., Weisz D. R., Skillman E. D., Fouesneau M., Dolphin A. E., 2015, ApJ, 810, 9
D'Agostino J. J., Poetrodjojo H., Ho I. T., Groves B., Kewley L., Madore B. F., Rich J., Seibert M., 2018, MNRAS, 479, 4907
D'Onghia E., Vogelsberger M., Hernquist L., 2013, ApJ, 766, 34
Davies R. I., Sugai H., Ward M. J., 1997, Molecular Hydrogen Emission in NGC 4536, Technical Report, OUAST/97/15 Astrophysics Dept.
Davis B. L. et al., 2015, ApJ, 802, L13
de Vaucouleurs G., 1959, Handbuch der Physik, 53, 275
Dobbs C. L., Theis C., Pringle J. E., Bate M. R., 2010, MNRAS, 403, 625
Donner K. J., Thomasson M., 1994, A&A, 290, 785
Dopita M. A., Kewley L. J., Sutherland R. S., Nicholls D. C., 2016, Ap&SS, 361, 61
Egusa F., Sofue Y., Nakanishi H., 2004, PASJ, 56, L45
Egusa F., Kohno K., Sofue Y., Nakanishi H., Komugi S., 2009, ApJ, 697, 1870
Egusa F., Mentuch Cooper E., Koda J., Baba J., 2017, MNRAS, 465, 460
Elagali A. et al., 2019, MNRAS, 487, 2797
Elmegreen B. G., Galliano E., Alloin D., 2009, ApJ, 703, 1297
Fitzpatrick E. L., Massa D., Gordon K. D., Bohlin R., Clayton G. C., 2019, ApJ, 886, 108
Foyle K., Rix H. W., Dobbs C. L., Leroy A. K., Walter F., 2011, ApJ, 735, 101
Fujii M. S., Baba J., Saitoh T. R., Makino J., Kokubo E., Wada K., 2011, ApJ, 730, 109
Gaia Collaboration, 2016, A&A, 595, A1
Garcia A. M. et al., 2023, MNRAS, 519, 4716
Gittins D. M., Clarke C. J., 2004, MNRAS, 349, 909
Grand R. J. J., Kawata D., 2016, Astron. Nachr., 337, 957
Grand R. J. J., Kawata D., Cropper M., 2012, MNRAS, 426, 167
Grand R. J. J., Kawata D., Cropper M., 2015, MNRAS, 447, 4018
Grand R. J. J. et al., 2016, MNRAS, 460, L94
Grasha K. et al., 2022, ApJ, 929, 118
Gurzadyan G. A., 1997, The Physics and Dynamics of Planetary Nebulae. Springer-Verlag, Berlin Heidelberg, New York
Hess K. M., Pisano D. J., Wilcots E. M., Chengalur J. N., 2009, ApJ, 699, 76
Ho I. T., 2016, Astrophysics Source Code Library, record ascl:1607.018
Ho I.-T. et al., 2016, Ap&SS, 361, 208
Ho I.-T. et al., 2017, ApJ, 846, 39
Ho I. T. et al., 2018, A&A, 618, A64
Honma M., Nagayama T., Sakai N., 2015, PASJ, 67, 70
Jarrett T. H., Chester T., Cutri R., Schneider S. E., Huchra J. P., 2003, AJ, 125, 525
Jarrett T. H. et al., 2013, AJ, 145, 6
Jorsater S., van Moorsel G. A., 1995, AJ, 110, 2037

[8] http://www.astropy.org
[9] https://datacentral.org.au/

Kauffmann G. et al., 2003, MNRAS, 346, 1055
Kennicutt Robert C. J., 1998, ARA&A, 36, 189
Kewley L. J., Dopita M. A., Sutherland R. S., Heisler C. A., Trevena J., 2001, ApJ, 556, 121
Kewley L. J., Nicholls D. C., Sutherland R. S., 2019, ARA&A, 57, 511
Khoperskov S., Sivkova E., Saburova A., Vasiliev E., Shustov B., Minchev I., Walcher C. J., 2023, A&A, 671, A56
Kreckel K. et al., 2019, ApJ, 887, 80
Kumari N., Maiolino R., Belfiore F., Curti M., 2019, MNRAS, 485, 367
Lamastra A. et al., 2016, A&A, 596, A68
Leroy A. K. et al., 2019, ApJS, 244, 24
Li Z., Krumholz M. R., Wisnioski E., Mendel J. T., Kewley L. J., Sánchez S. F., Galbany L., 2021, MNRAS, 504, 5496
Lin C. C., Shu F. H., 1964, ApJ, 140, 646
Lindblad P. A. B., Lindblad P. O., Athanassoula E., 1996, A&A, 313, 65
Lintott C. J. et al., 2008, MNRAS, 389, 1179
Maiolino R., Mannucci F., 2019, A&AR, 27, 3
Malin D., Hadley B., 1997, Publ. Astron. Soc. Aust., 14, 52
Martínez-García E. E., 2012, ApJ, 744, 92
Martínez-García E. E., González-López lira R. A., Bruzual-A G., 2009, ApJ, 694, 512
Meidt S. E. et al., 2013, ApJ, 779, 45
Mihos J. C., Bothun G. D., 1997, ApJ, 481, 741
Minchev I., Famaey B., 2010, ApJ, 722, 112
Minchev I., Famaey B., Combes F., Di Matteo P., Mouhcine M., Wozniak H., 2011, A&A, 527, A147
Oh S. H., Kim W.-T., Lee H. M., Kim J., 2008, ApJ, 683, 94
Oh S. H., Kim W.-T., Lee H. M., 2015, ApJ, 807, 73
Orr M. E. et al., 2023, MNRAS, 521, 3708
Osterbrock D. E., 1989, Astrophysics of Gaseous Nebulae and Active Galactic Nuclei. University Science Book, Mill Valley, CA
Pan Y. C., Foley R. J., Jones D. O., Filippenko A. V., Kuin N. P. M., 2020, MNRAS, 491, 5897
Pancoast A., Sajina A., Lacy M., Noriega-Crespo A., Rho J., 2010, ApJ, 723, 530
Peterken T. G., Merrifield M. R., Aragón-Salamanca A., Drory N., Krawczyk C. M., Masters K. L., Weijmans A.-M., Westfall K. B., 2019, Nat. Astron., 3, 178
Pettitt A. R., Tasker E. J., Wadsley J. W., 2016, MNRAS, 458, 3990
Pettitt A. R., Tasker E. J., Wadsley J. W., Keller B. W., Benincasa S. M., 2017, MNRAS, 468, 4189
Pettitt A. R., Wadsley J. W., 2018, MNRAS, 474, 5645
Pfleiderer J., Siedentopf H., 1961, Z. Astrophys., 51, 201
Pikel'Ner S. B., 1965, SvA, 9, 408
Pilyugin L. S., Grebel E. K., 2016, MNRAS, 457, 3678
Poetrodjojo H., D'Agostino J. J., Groves B., Kewley L., Ho I. T., Rich J., Madore B. F., Seibert M., 2019, MNRAS, 487, 79
Pohlen M., Martínez-Delgado D., Majewski S., Palma C., Prada F., Balcells M., 2004, in Prada F., Martinez Delgado D., Mahoney T. J., eds, ASP Conf. Ser. Vol. 327, Satellites and Tidal Streams. Astron. Soc. Pac., San Francisco, p. 288
Pour-Imani H., Kennefick D., Kennefick J., Davis B. L., Shields D. W., Shameer Abdeen M., 2016, ApJ, 827, L2
Prantzos N., Boissier S., 2000, MNRAS, 313, 338
Puerari I., Dottori H., 1997, ApJ, 476, L73
Qu Y., Di Matteo P., Lehnert M. D., van Driel W., Jog C. J., 2011, A&A, 535, A5
Rosario D. J., Mendel J. T., Ellison S. L., Lutz D., Trump J. R., 2016, MNRAS, 457, 2703
Rots A. H., Shane W. W., 1975, A&A, 45, 25
Rozas M., Knapen J. H., Beckman J. E., 1996, A&A, 312, 275
Ryder S. D., Walsh W., Malin D., 1999, Publ. Astron. Soc. Aust., 16, 84
Sánchez S. et al., 2015a, Galaxies, 3, 164
Sánchez S. F. et al., 2015b, A&A, 573, A105
Sánchez-Gil M. C., Jones D. H., Pérez E., Bland-Hawthorn J., Alfaro E. J., O'Byrne J., 2011, MNRAS, 415, 753
Sánchez-Menguiano L. et al., 2016, ApJ, 830, L40
Sánchez-Menguiano L. et al., 2018, A&A, 609, A119
Sánchez-Menguiano L., Sánchez S. F., Pérez I., Ruiz-Lara T., Galbany L., Anderson J. P., Kuncarayakti H., 2020, MNRAS, 492, 4149
Santoro F. et al., 2022, A&A, 658, A188
Savchenko S., Marchuk A., Mosenkov A., Grishunin K., 2020, MNRAS, 493, 390
Scarano S., Lépine J. R. D., 2013, MNRAS, 428, 625
Schinnerer E. et al., 2013, ApJ, 779, 42
Sellwood J. A., Binney J. J., 2002, MNRAS, 336, 785
Sellwood J. A., Carlberg R. G., 1984, ApJ, 282, 61
Sextl E. et al., 2024, ApJ, 960, 83
Shabani F. et al., 2018, MNRAS, 478, 3590
Shapley A. E. et al., 2019, ApJ, 881, L35
Sharda P., Ginzburg O., Krumholz M. R., Forbes J. C., Wisnioski E., Mingozzi M., Zovaro H. R. M., Dekel A., 2024, MNRAS, 528, 2232
Shu F. H., 2016, ARA&A, 54, 667
Silva-Villa E., Larsen S. S., 2012, A&A, 537, A145
Simpson C., Wilson A. S., Bower G., Heckman T. M., Krolik J. H., Miley G. K., 1997, ApJ, 474, 121
Slater R. et al., 2019, A&A, 621, A83
Spitoni E., Cescutti G., Minchev I., Matteucci F., Silva Aguirre V., Martig M., Bono G., Chiappini C., 2019, A&A, 628, A38
Struck C., Dobbs C. L., Hwang J.-S., 2011, MNRAS, 414, 2498
Sundelius B., Thomasson M., Valtonen M. J., Byrd G. G., 1987, A&A, 174, 67
Tinsley B. M., Larson R. B., 1978, ApJ, 221, 554
Toomre A., 1969, ApJ, 158, 899
Toomre A., 1977, ARA&A, 15, 437
Toomre A., Toomre J., 1972, ApJ, 178, 623
Vazdekis A., Ricciardelli E., Cenarro A. J., Rivero-González J. G., Díaz-García L. A., Falcón-Barroso J., 2012, MNRAS, 424, 157
Vogt F. P. A., Pérez E., Dopita M. A., Verdes-Montenegro L., Borthakur S., 2017, A&A, 601, A61
Werk J. K., Putman M. E., Meurer G. R., Thilker D. A., Allen R. J., Bland-Hawthorn J., Kravtsov A., Freeman K., 2010, ApJ, 715, 656
Willett K. W. et al., 2013, MNRAS, 435, 2835
Yu S.-Y., Ho L. C., 2019, ApJ, 871, 194
Zhang K. et al., 2017, MNRAS, 466, 3217

APPENDIX A: Σ_{SFR} MAPS AND $\Delta\Sigma_{SFR}$ MAPS

The maps of Σ_{SFR} and $\Delta\Sigma_{SFR}$ are shown in Fig. A1.

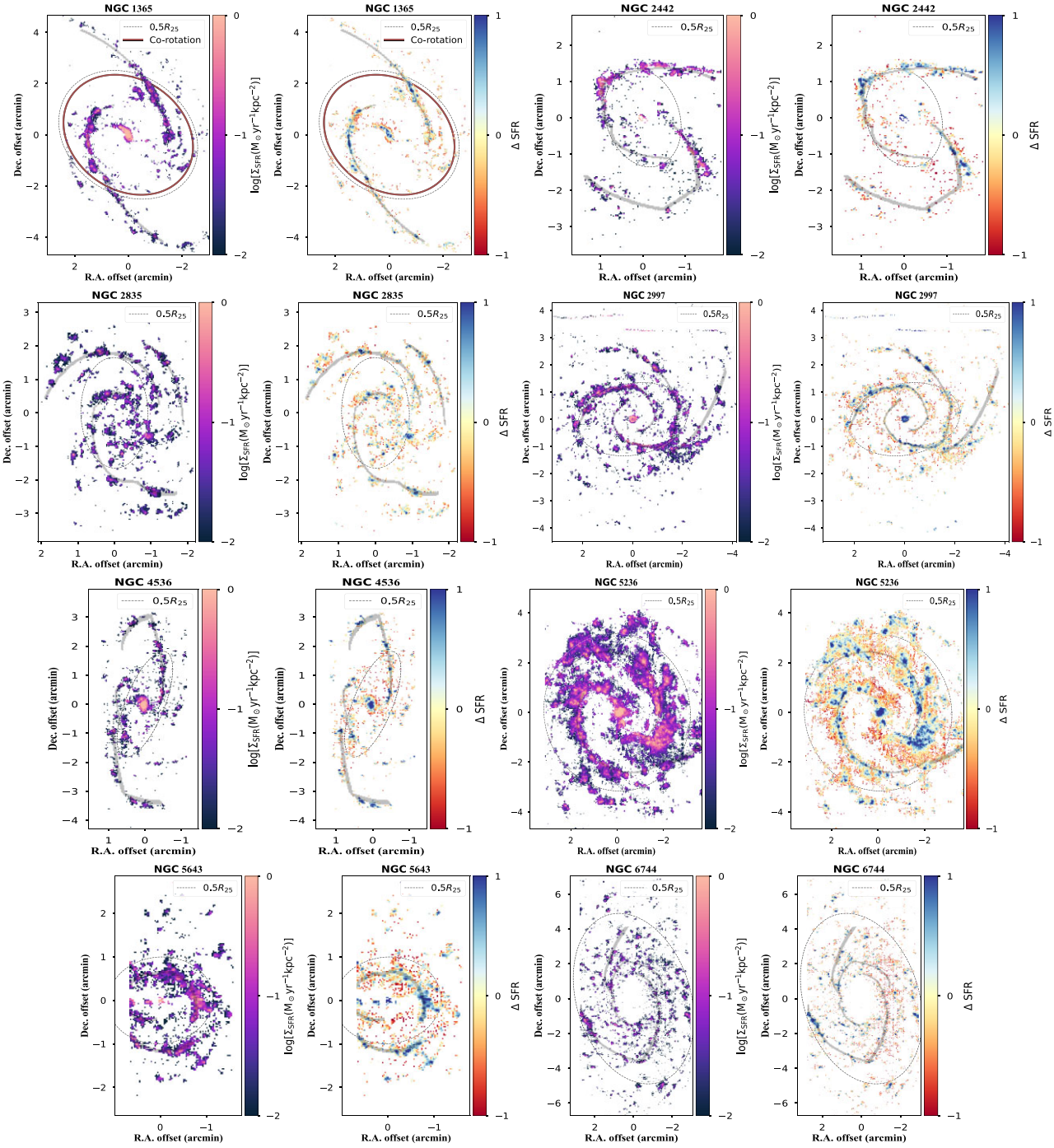

Figure A1. Columns 1 and 3: 2D Σ_{SFR} maps of our galaxies, except for NGC 1566 (Fig. 4). Columns 2 and 4: residual of Σ_{SFR} by subtracting the radial gradients. More detail on this analysis is in Section 3.4. The dashed ellipse marks the location of half R_{25} and the red ellipse denotes the CR, if applicable.

APPENDIX B: 12 + LOG(O/H) MAPS AND Δlog(O/H) MAPS

The maps of 12 + log(O/H) and Δlog(O/H) are shown in Fig. B1.

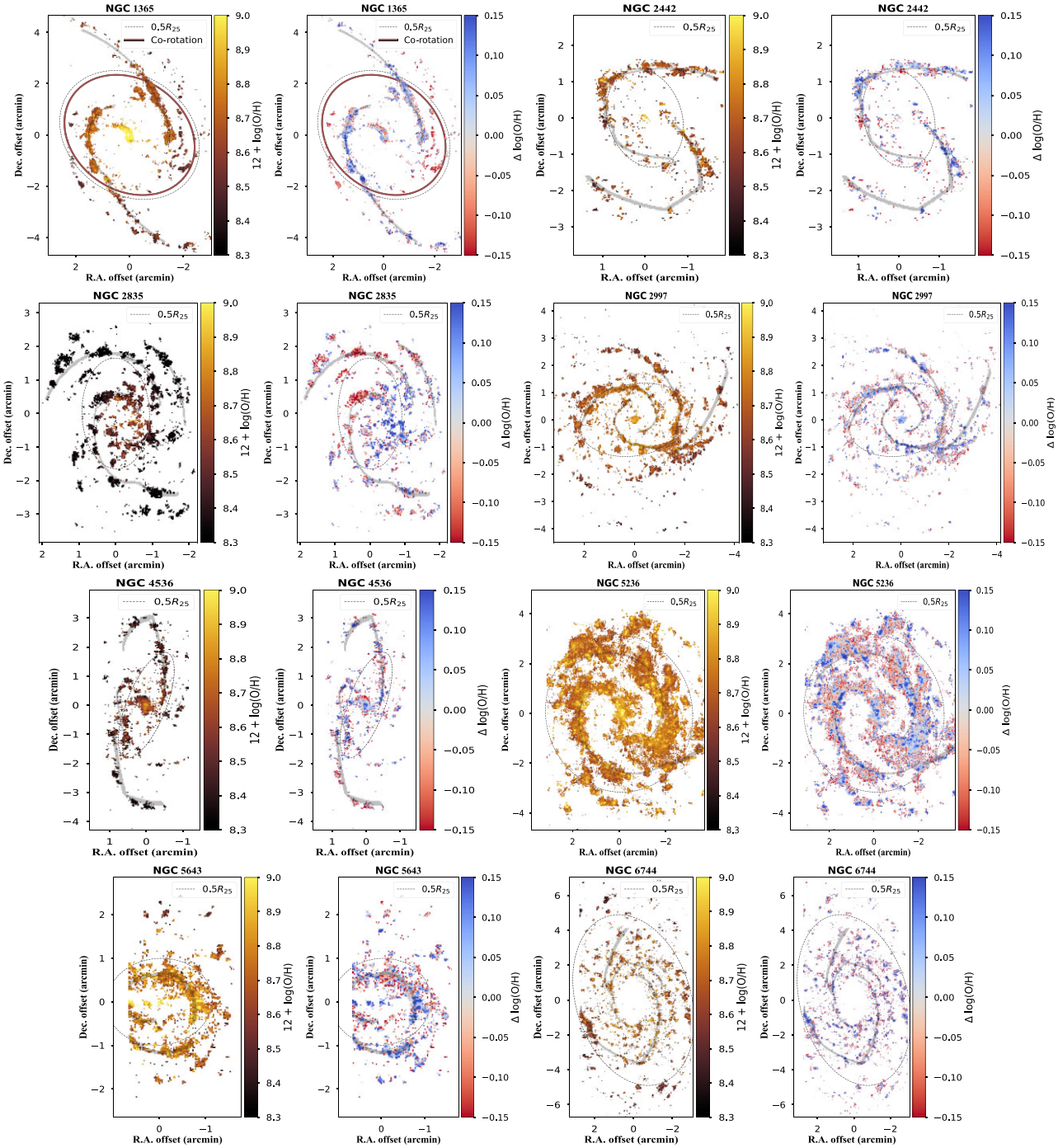

Figure B1. Columns 1 and 3: 2D 12 + log(O/H) maps of our galaxies, except for NGC 1566 (Fig. 5). Columns 2 and 4: residual of metallicity (Δlog(O/H)) by subtracting the radial gradients. The dashed ellipse marks the location of half R_{25} and the red ellipse denotes the CR, if applicable. More detail on this analysis is in Section 3.4.

APPENDIX C: GAS-PHASE METALLICITY WITH S-CAL CALIBRATION

In the main text, we use N_2S_2–$N_2H\alpha$ diagnostic from D16 to determine the gas-phase metallicity of our spiral galaxies. As the physical resolution of our sample ranges from 145 to 39 pc, comparable to the typical size of H II region, it is a caveat that the metallicities of some spaxels are contaminated by DIG. Poetrodjojo et al. (2019) find that all diagnostics are affected by the inclusion of DIG. As the current knowledge about modelling metallicity in DIG is still limited (Kewley, Nicholls & Sutherland 2019), we cannot separately derive the metallicity in the DIG.

Emission lines in DIG are excited by ionized photons leaked from H II regions and low-mass evolved stars. To test the impact of DIG

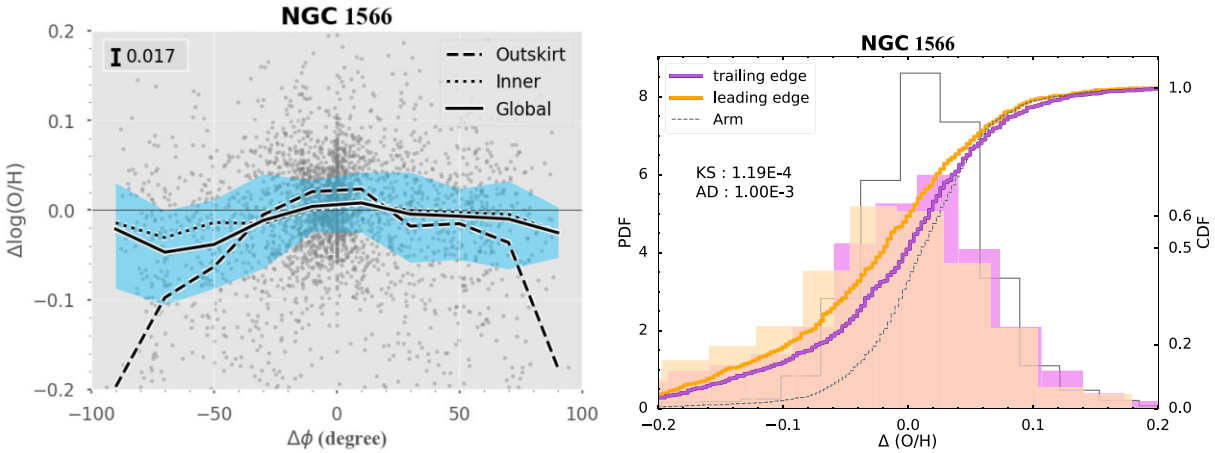

Figure C1. Left: density scatter plot of metallicity residual $\Delta\log(O/H)$ versus azimuthal distance to the spiral arms $\Delta\phi$. $\Delta\log(O/H)$ is calculated by subtracting the radial gradient from the Scal metallicity. $\Delta\phi$ is the same as Fig. 3, described in Section 3.3. We find slightly higher $\Delta\log(O/H)$ in the trailing edge ($\Delta\phi > 0$) than the leading edge ($\Delta\phi < 0$), similar with the main results using N_2S_2–$N_2H\alpha$ diagnostic (Fig. 7). Right: comparing the CDFs of $\Delta\log(O/H)$ from Scal among the trailing edge, leading edge, and spiral arms. The p-value from the KS and AD tests are shown in the upper left. We find higher $\Delta\log(O/H)$ in the trailing edge, with a p-value of 1.19×10^{-4}, suggesting that the metallicity on both sides of the spiral arms are drawn from different distributions.

in our results, we adopt S-calibration (Scal) from Pilyugin & Grebel (2016) which relies on three standard diagnostic lines:

$$R_2 = I_{[\mathrm{O\,III}]\lambda4959+\lambda5007}/I_{\mathrm{H}\beta},$$
$$N_2 = I_{[\mathrm{N\,II}]\lambda\lambda6548,84}/I_{\mathrm{H}\beta},$$
$$S_2 = I_{[\mathrm{S\,II}]\lambda\lambda6717,31}/I_{\mathrm{H}\beta}. \quad \text{(C1)}$$

The inclusion of three emission-line ratios allows Scal to be corrected for the dependence on ionization parameter (Pilyugin & Grebel 2016).

We take NGC 1566 for an explanation in this section. The left panel of Fig. C1 shows the fluctuation of metallicity residual $\Delta\log(O/H)$ when crossing the spiral arms, with positive $\Delta\phi$ indicating the trailing edge. We use the same definition of $\Delta\phi$ in the main test, shown in Fig. 3 and described in Section 3.3. The moving medians of each 20° $\Delta\phi$ are shown as a solid black line, with 25 per cent and 75 per cent quantiles as blue shadows. We repeat the calculation of moving medians to the inner and outer regions, with each region containing half of the spaxels. Similar to the result from N_2S_2–$N_2H\alpha$ (Fig. 7), we find slightly lower metallicity in the leading edge ($\Delta\phi < 0$) in NGC 1566 using Scal (Fig. C1). The magnitude of the azimuthal variation and the metallicity scattering from Scal are smaller than those from N_2S_2–$N_2H\alpha$, which is expected (Pilyugin & Grebel 2016; Kreckel et al. 2019).

We further compare the metallicity distributions on both sides of the spiral arms by applying the KS and AD tests to their CDFs. Both tests reject that the metallicity distribution in the leading and trailing edges are drawn from the same parental distribution. Although Scal brings in a smaller intrinsic scatter, we obtain a D-value of 0.127 from the Scal CDFs, comparable to the D-value from N_2S_2–$N_2H\alpha$. We observe azimuthal variation in the metallicity of NGC 1566 in both Scal and N_2S_2–$N_2H\alpha$ diagnostics. The highly similar trend of $\Delta\log(O/H)$ along $\Delta\phi$ suggests the limited impacts of DIG on our TYPHOON data.

This paper has been typeset from a TEX/LATEX file prepared by the author.